Effect of Magnetic Islands on the Local Plasma Behavior in a Tokamak

Erik Dannel Taylor

Submitted in partial fulfillment of the
requirements for the degree
of Doctor of Philosophy
in the Graduate School of Arts and Sciences

COLUMBIA UNIVERSITY

2000

ABSTRACT

Effect of Magnetic Islands on the Local Plasma Behavior in a Tokamak

Erik Dannel Taylor

Experiments on the HBT-EP (High Beta Tokamak-Extended Pulse) tokamak provided local measurements of the pressure and ion velocity perturbations from rotating magnetic island using Mach probes. The presence of magnetic islands created two distinct features in ion fluid velocity measurements. First, the toroidal velocity profile was sharply peaked near the center of the 2/1 magnetic island. Second, the ion velocity near this island was only ~30% of the magnetic island velocity. Measurements of the perturbations from rotating magnetic islands with stationary detectors prompted the development of a new data analysis technique using the Hilbert transform. This method generated plots of the pressure profile co-rotating with the magnetic island, allowing the analysis of the pressure profile behavior at the O and X-points of the magnetic island. Experiments with active rotation control demonstrated that the pressure perturbations followed the magnetic island motion, while simultaneously measuring that the ion velocity and acceleration were less that those of the magnetic island. These observations agreed with predictions from a two-fluid plasma model that included the effect of magnetic islands on the diamagnetic velocity as well as neutral damping effects. Understanding the effect of magnetic islands on the pressure and ion velocity profiles is crucial for both fundamental plasma studies and the development of more efficient tokamaks using advanced tokamak (AT) concepts.

Chapter 1. The Fusion Problem

Section 1.1. The role of fusion in energy production

Nuclear fusion attempts to offer a meaningful alternative source of energy [Wesson, 1997]. Fusion uses the popularized relation $E = mc^2$ to convert mass m into energy E, where c is the speed of light in a vacuum. The division point between fusion and fission reactions occurs at Ni^{62}. Fusion releases energy for lighter reactants, and fission releases energy for heavier elements. The complexity of fusion reactors present challenges for the production of energy. Fusion reactors lack the years of experience and process refinement that have gone into other energy systems such as oil, coal, gas, and hydroelectric power. This deficiency can be overcome by operating fusion at large scales or in specialized situations where the need for energy justifies the expense. A large-scale power plant could potentially replace or complement coal, hydroelectric, and nuclear plants powering large metropolitan and industrial areas. Pollution reduction at a large scale will help offset the technical challenges in implementing a new energy system. Fusion could also replace fission reactors in systems that require independence from the need to regularly refuel.

Fusion as a power system overcomes some of the drawbacks of other energy production techniques. The key disadvantages of fossil fuels are the limited supply and pollution created by the power production. Hydroelectric power requires the damming of rivers, entailing substantial environment impact. Fusion avoids the pollution issues by using a source of energy with an extremely high output, thereby reducing the fuel

requirements and the resulting pollution. Fusion also overcomes some of the radiation hazard inherent in nuclear fission. Although tritium is radioactive, the decay process and the decay products are significantly less hazardous than is the case for fission. The remaining techniques of solar and wind power are excellent methods for supplementing day-to-day power needs, and aiding the operation of highly mobile off-gird systems. However, neither holds the prospect of meeting large-scale energy demands. Fusion is the only alternative that offers high output combined with low pollution levels and low fuel requirements.

Section 1.2. How nuclear fusion works

A substantial energy barrier opposes fusion reactions. The long range Coulomb repulsion between the nuclei offsets the attractive strong nuclear force. The problem is one of bringing the nuclei sufficiently close for the strong nuclear force to overcome the Coulomb barrier. The cross section combines the effects of the potential barrier and thermal velocity distribution of the nuclei into an effective area for fusion collisions. The cross section forms an equation

(1.1) $f_{fusion} = n\sigma v$,

where n is the density of nuclei, σ is the cross section, v is the thermal velocity, and f_{fusion} is the frequency of fusion producing collisions. Increasing any of these three quantities will increase the collision frequency. The cross section is also itself a function of thermal energy in the nuclei. The cross section increases from virtually zero at room temperatures up to feasible magnitudes at temperatures of $\sim 10-100$ keV. At these temperature levels, the fusion reactants exist in a plasma state.

Both the net output energy and the reaction cross section govern the choice of reactants for the fusion process. The favored choice for the reaction is

(1.2) $D + T \rightarrow He^4 + n + 17.6 \text{ MeV}$,

where the deuterium and tritium isotopes of hydrogen fuse to produce a helium atom and a neutron. The helium atom contains $3.5\,MeV$ of the released kinetic energy, while the neutron has the remaining $14.1\,MeV$. The cross section for this reaction is several orders of magnitude larger than the other possible options. The deuterium and tritium reactions offer the best combination of high output energy and high cross section.

The feasibility of the deuterium-tritium reaction is also a function of the availability of these fuels. Deuterium is a naturally occurring isotope of hydrogen. Although only one hydrogen atom in 6700 is the deuterium isotope, the massive amounts of hydrogen available in seawater offset the rarity. Tritium, with a half-life of only 12.3 years, does not occur in nature. However, tritium can be bred using either of two reactions

(1.3) $Li^6 + n \rightarrow T + He^4 + 4.8\,MeV$, or

(1.4) $Li^7 + n \rightarrow T + He^4 + n - 2.5\,MeV$.

The amount of lithium available throughout the world could potentially supply the world power needs for $\sim 10^6$ years [Wesson, 1997].

Section 1.3. Plasmas in fusion

Raising the temperature of a gas to fusion levels converts the reactants into plasma. Plasma is an ionized gas where the bound electrons are released from the neutral

atoms, creating free electrons and ions. These particles interact electrically through the Coulomb force

$$\mathbf{F} = \frac{1}{4\pi\varepsilon_0}\frac{q_1 q_2}{r^2}\hat{\mathbf{r}}, \tag{1.5}$$

where $\mathbf{F}$ is the force, ε_0 is the permeability of free space, q_1 and q_2 are the magnitude of the interacting charges, and r is the radius separating them. This equation critically determines the behavior of the plasma. The most important feature is the long-range nature of the Coulomb interaction. This long-range force causes the ions and electrons to act collectively; creating the novel behavior that is the focus of plasma science research.

The primary research challenge in nuclear fusion is achieving plasma confinement. Collisions serve to randomize the motion of the plasma particles, allowing the transport of plasma out of the confinement region. This transport reduces the density and temperature of the plasma, and hence reduces the fusion output. One method of plasma confinement is to use a magnetic field. This field reduces the step size of the random motion due to collisions, allowing plasma confinement over many particle collisions.

Section 1.4. Basis for magnetic confinement

The basis for magnetic confinement stems from the response of charged particles to magnetic fields. The Lorentz force law describes the reaction of a single charged particle to electric and magnetic fields [Chen, 1984]

$$\mathbf{F} = q\left(\mathbf{E} + \mathbf{v}\times\mathbf{B}\right). \tag{1.6}$$

For the electric field, the force is along the field line and depends only on the local electric field and particle charge. For magnetic fields however, the force is orthogonal to the field, and the magnitude and direction depend on the particle velocity. Solving the force equation for the motion of a single particle in a magnetic field derives two different behaviors, one along the field line, and one orthogonal to the field. Along the magnetic field the cross product of the velocity and magnetic field is zero, producing no force. The particle can freely streaming along the field, acting as though the field was not present. Orthogonal to the magnetic field, the particle undergoes circular orbits, known as cyclotron motion. This cyclotron motion provides the basis of magnetic confinement. During collisions, the random step size of the particles is on the order of this orbit radius, known as the gyro radius. By taking the magnetic field line and wrapping it into a loop, the particles will freely stream along the loop. Orthogonal to the field the plasma particles will orbit the field lines until undergoing a collision, when the step size will be on the order of the gyro-radius. Strengthening the magnetic field decreases this radius, and hence reduces the plasma transport. This method is known as toroidal confinement.

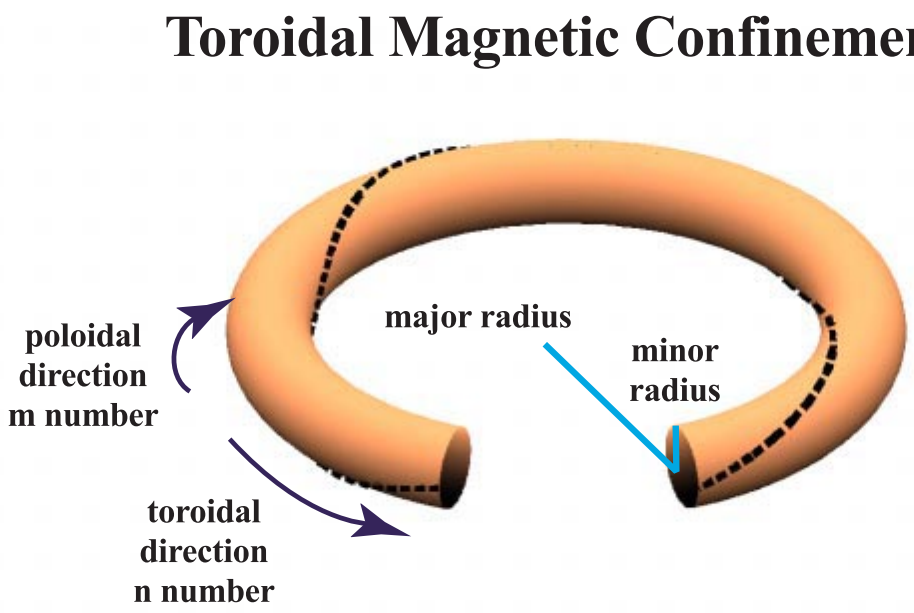

Figure 1.1: Toroidal coordinate system.

Toroidal confinement constructs a toroidal geometry for the plasma and magnetic field (Fig. 1.1). The two key directions are the long way around the torus, known as the toroidal direction, and the short way around the torus, known as the poloidal direction. In addition to these directions, there are two key radii that help locate the position and size of the plasma. The distance from the axis of the entire torus to the point of interest is the major radius. The minor radius gives the distance from the center of the bulk of the torus to the point of interest.

Early magnetic fusion studies determined that both toroidal and poloidal fields are necessary to stability confine a plasma [Friedberg, 1987]. A range of options exists for generating these two fields. Magnetic fields may be generated either by currents driven

in external coils or by currents in the plasma. The different confinement techniques can be organized on a scale of increasing dependence on plasma self-organization. At the lowest level, both the toroidal and poloidal fields can be generated by external coils, producing a stellarator. The next step is to a tokamak, where external coils generate the strong toroidal field, while the toroidal plasma current generates the weaker poloidal field. Reducing the strength of the external toroidal field converts the tokamak into a reverse field pinch (RFP), where the plasma current and external coils generate roughly equal amounts of magnetic field. Finally, the spheromak depends almost entirely on internal currents to generate both the toroidal and poloidal magnetic fields.

Section 1.5. Importance of magnetic islands

One of the major limitations on the performance of fusion devices is the presence of plasma instabilities. Magnetic islands are a particularly important limiting instability in the performance of a wide range of tokamaks [Sauter, 1997]. These islands alter the overall magnetic field topology, degrading the plasma confinement. This degradation can lead to both disruptions and increased plasma transport far above the collisionally driven transport levels. In addition, the magnetic islands radially connect plasma regions at different temperatures and densities. Because magnetic fields produce no force on particles moving along the field, the different plasmas will rapidly mix together, assuming the average value for the pressure. This mixing flattens the radial pressure profile.

Magnetic islands are not confined solely to tokamaks. Islands have also been measured in stellarators [Jaenicke, 1988] and RFPs [Hartog, 1999]. The prevalence of

magnetic islands across a wide range of fusion devices demonstrates that islands are an intrinsic problem associated with the present of plasma current. The elimination of the islands requires an active control technique to suppress the instability during the plasma discharge.

One suppression technique of considerable interest is active rotation control [Mauel, in press; Navratil, 1998; Morris, 1990; Smoylakov, 1995; Kurita, 1992]. Magnetic islands generally rotate around fusion devices at the kilohertz range of frequencies. The island rotation interacts with the background plasma to produce rotating perturbations in the plasma pressure and velocity profiles. Active rotation control attempts to use this interaction to produce damping forces that induce a reduction in the island size [Kurita, 1992; Jensen, 1993; Yokoyama, 1996]. The external control system alters the island motion, which then in turn changes the plasma behavior. Understanding how the magnetic islands interact with the plasma, particularly with the ion fluid velocity, is crucial to understanding and improving rotation control techniques.

Chapter 2. Two-Fluid Plasma Model and Magnetic Islands

Section 2.1. The fluid plasma model

Plasma behavior encompasses both the plasma response to electric and magnetic fields as well as the fluid pressure effect from the surrounding plasma. The two-fluid plasma model treats the ions and electrons as separate fluids using the equation [Braginskii, 1965; Chen, 1984]

$$m_\alpha n \frac{d\mathbf{v}_\alpha}{dt} = q_\alpha n(\mathbf{E} + \mathbf{v}_\alpha \times \mathbf{B}) - \nabla p_\alpha , \quad (2.1)$$

where α denotes the species. The first term describes the inertial response from the species of mass m_α, density n, and acceleration $\frac{d\mathbf{v}_\alpha}{dt}$. The next two terms describe the Lorentz response of the fluid comprised of particles with charge q_α to the electric and magnetic fields, $\mathbf{E}$ and $\mathbf{B}$ respectively. The final term describes the force due to gradients in the pressure,

$$p_\alpha = nT_\alpha , \quad (2.2)$$

where T_α is the species temperature.

The two-fluid equations can be used to derive a relationship between the electric field, pressure gradient and fluid velocity. The inertial term in Eq. 2.1 gives rise to cyclotron motion around the magnetic field. This motion has a mean velocity of zero, so this term may be ignored for fluid velocity calculations. Taking the cross product of the remaining terms in Eq. 2.1 with $\mathbf{B}$ gives the equation

$$\mathbf{v}_\perp = \frac{\mathbf{E}\times\mathbf{B}}{B^2} - \frac{\nabla p_\alpha \times \mathbf{B}}{q_\alpha n B^2}, \quad (2.3)$$

where $\mathbf{v}_\perp$ is the velocity orthogonal to the magnetic field. Both electric fields and pressure gradients generate fluid motion. The $\mathbf{E}\times\mathbf{B}$ electric field term is independent of the fluid charge, and therefore is in the same direction for both the ion and electron fluids. The second term, known as the diamagnetic term, is a function of the charge and hence points in the opposite direction for the two fluids.

In tokamaks, the variation in the strength of the toroidal magnetic field with major radius dampens the plasma flow in the poloidal direction [Stix, 1973]. For tokamaks, $\mathbf{B}$ points largely in the toroidal direction, and hence $\mathbf{v}_\perp$ points in the poloidal direction. Since $|\mathbf{B}| \sim |\mathbf{B}_T|$, Eq. 2.3 becomes

$$|\mathbf{v}_\perp| = \frac{E_r}{B_T} - \frac{\nabla p_{\alpha_r}}{q_\alpha n B_T}. \quad (2.4)$$

However, this expectation disagrees with velocity measurements in tokamaks that have observed large toroidal and small poloidal flow [LaHaye, 1993; LaHaye, 1994]. This discrepancy can be attributed to the major radial variation in magnetic field strength [Stix, 1973]. The current in the toroidal field coils generates a magnetic field varying as

$$B \sim \frac{1}{R}, \quad (2.5)$$

where R is the major radius [Griffiths, 1989]. As B increases, the plasma undergoes magnetic pumping, which is theorized to introduce a strong dissipation from ion viscosity, reducing the poloidal flow [Stix, 1973]. Both theory and measurements [LaHaye, 1993; LaHaye, 1994] indicate that the poloidal velocity will be small.

Although magnetic pumping dampens the flow orthogonal to the magnetic field, it does not impede fluid motion parallel to the magnetic field. This motion can compensate for poloidal damping by providing an equivalent velocity as the fluid moves along the magnetic field. In a torus, two flux functions, the field-aligned flow and the toroidal flow can describe the mass flow. In neo-classical theory, the field-aligned flow is the poloidal flow and is strongly damped, leaving only the toroidal flow [Stix, 1973; Hirshman, 1981]. Because the magnetic field contains both a toroidal and poloidal component, motion along the field produces a toroidal and poloidal displacement. The projection of a large parallel velocity can produce a net poloidal velocity equal to that driven by the electric and pressure gradient forces. This motion sharply increases the predicted toroidal velocity according to the following equation where $v = |\mathbf{v}|$ [Kluber, 1991; deVries, 1997]

$$(2.6) \quad v_T \sim v_{||} = \frac{B_T}{B_P} \cdot v_{\perp} = \frac{E_r}{B_p} + \frac{1}{qnB_p} \frac{\partial p}{\partial r}.$$

Because a torus is a closed system, the velocity corresponds to motion around a circle, and is equivalent to frequency. The toroidal velocity can be converted into a frequency of rotation ω_α using the relation

$$(2.7) \quad \omega_\alpha = \frac{v_T}{2\pi R}.$$

The electric field and diamagnetic terms can similarly be transformed into frequencies, producing the equation

$$(2.8) \quad \omega_\alpha = \omega_E + \omega_{*\alpha},$$

where the electric field term is

$$(2.9) \quad \omega_E = \frac{1}{2\pi R} \frac{E_r}{B_p},$$

and the diamagnetic term for the species α is

(2.10) $\omega_{*\alpha} = \pm \frac{1}{2\pi R} \frac{\nabla p_\alpha}{q_\alpha n B_p}$.

Section 2.2. Effect of neutral damping on plasma behavior

The presence of neutral particles can dampen the plasma velocity [Braginskii, 1965; Rowan, 1993]. Neutral particles can be converted into plasma particles by either charge exchange or ionization reactions [Eletsky, 1983]. When a neutral particle is ionized, the new particle appears with effectively zero velocity, thereby reducing the momentum in the plasma. In charge exchange reactions, the electron from the neutral transfers to a plasma ion, replacing the fast ion with a new cold, stationary one

(2.11) $A + B^+ \rightarrow A^+ + B$.

This process substantially dampens the ion velocity, as it completely removes the original ion momentum from the plasma, producing a large slowing of the ion velocity. The dominance of the charge-exchange reaction in reducing the ion velocity stems from the large ion mass [Braginskii, 1965]. After losing its momentum, an ion is much slower to return to its former velocity than an electron. When acted on by a force, such as the electric and diamagnetic forces driving fluid motion, the electron acceleration a_e is a mass ratio larger than the ion acceleration a_{ion}

(2.12) $\frac{a_e}{a_{ion}} \approx \frac{m_{ion}}{m_e} = 3627$.

Work on the TEXT tokamak developed a term in the ion velocity equation that incorporated neutral damping effects [Rowan, 1993]. The model assumes that the neutral

particles have essentially zero velocity compared to the ions. The charge exchange removes the ion momentum from the system and introduces a new stationary ion. The model reduces the prediction of Eq. 2.8 by a factor F_{cx} [Rowan, 1993; Valanju, 1992]

(2.13) $\omega_i = F_{cx}\omega_{i\,\mathrm{No\,CX}} = F_{cx}\left(\omega_E - \omega_{*i}\right)$.

F_{cx} ranges in value from $0 \le F_{cx} \le 1$, where one corresponds to no effect from the neutrals (typically due to full ionization), and zero corresponds to the complete suppression of the flow (from high neutral densities). Theoretical work [Valanju, 1992; Rowan, 1993] suggested F_{cx} has the form

(2.14) $$F_{cx} = \frac{1}{1 + \frac{2}{\pi}\left(\frac{R}{r}\right)^2 \frac{\nu_{cx}}{\omega_{transit}}},$$

where ν_{cx} is the charge exchange frequency and $\omega_{transit}$ is the transit frequency [Bell, 1979]

(2.15) $$\omega_{transit} = \frac{\sqrt{\frac{T_i}{M}}}{R\,q_s}.$$

The charge exchange frequency is function of the charge exchange cross section and the neutral particle number. The cross section is a weak function of temperature, being roughly constant for the temperatures typical of HBT-EP. Experiments on the TEXT tokamak demonstrated that charge exchange significantly altered the velocity profile [Rowan, 1993].

Section 2.3. Interaction between magnetic islands and the plasma fluid

The two equations for the electron and ion fluids can be combined to form a force balance equation and a generalization of Ohm's law. The large mass difference between the electrons m_e and the deuterium atoms m_D forming the plasma

$$\frac{m_D}{m_e} = 3672, \tag{2.16}$$

allows the use of approximations for the plasma mass density, velocity, and current respectively

$$\begin{aligned} \rho &= Mn_i + mn_e \approx n(M+m), \\ \mathbf{v} &= \frac{1}{\rho}(Mn_i\mathbf{v}_i + mn_e\mathbf{v}_e) \approx \frac{M\mathbf{v}_i + m\mathbf{v}_e}{M+m}, \\ \mathbf{j} &= e(n_i\mathbf{v}_i - n_e\mathbf{v}_e) \approx ne(\mathbf{v}_i - \mathbf{v}_e). \end{aligned} \tag{2.17}$$

Subtracting the two-fluid equations with the inclusion of resistive effects extends Ohm's law to treat plasmas

$$\mathbf{E} + \mathbf{v}\times\mathbf{B} = \eta\mathbf{j} + \frac{1}{en}(\mathbf{j}\times\mathbf{B} - \nabla p_e), \tag{2.18}$$

where η is the plasma resistivity. Substituting Eq. 2.17 in for the velocity and current, and then taking the curl of Eq. 2.18 gives

$$\frac{\partial\mathbf{B}}{\partial t} = \nabla\times(\mathbf{v}_e\times\mathbf{B}). \tag{2.19}$$

This equation states that the electron fluid moves with, or in standard plasma terminology is frozen to, the magnetic field lines. Motion of the magnetic field drags the electron fluid with it at the same velocity [Kluber, 1991]. Equation 2.19 links the motion of the magnetic field to the motion of the electron fluid.

Section 2.4. Formation of magnetic islands

Magnetic islands are an important limitation in the performance of tokamaks. The formation of magnetic islands requires the presence of resistivity in the plasma [Bateman, 1978; Friedberg, 1987]. The ideal Ohm's law precludes the change in the magnetic field required to form magnetic islands. The inclusion of even a very small amount of resistivity allows this topology change. If a region exists where the velocity $\mathbf{v}$, the field $\mathbf{B}$, or the cross product of the two is zero, then Ohm's law with resistivity (Eq. 2.18) becomes

(2.20) $\mathbf{E} \approx \eta \mathbf{j}$.

Taking the curl of this equation produces

(2.21) $$\frac{\partial \mathbf{B}}{\partial t} \approx \frac{\eta}{\mu_0} \nabla^2 \mathbf{B},$$

which is a diffusion equation for the magnetic field. Now, the field can diffuse, changing the overall magnetic field topology.

Section 2.5. Location of magnetic islands

The magnetic field tearing that creates magnetic islands in a tokamak can only occur at specific surfaces known as rational surfaces [Bateman, 1978]. The perturbation in the magnetic field can be expanded as

(2.22) $B \sim e^{ik_\varphi y - ik_\theta x}$.

At the tearing region

(2.23) $$\begin{aligned} &\mathbf{k} \cdot \mathbf{B} = 0, \\ &k_\varphi B_\varphi - k_\theta B_\theta = 0, \end{aligned}$$

$$k_\phi = \frac{n}{R}, \qquad k_\theta = \frac{m}{a}. \tag{2.24}$$

where m and n are integers. Defining a new quantity q measuring the pitch of the magnetic field

$$q = \frac{aB_\phi}{RB_\theta}. \tag{2.25}$$

Solving Equation 2.23 gives

$$q = \frac{m}{n}. \tag{2.26}$$

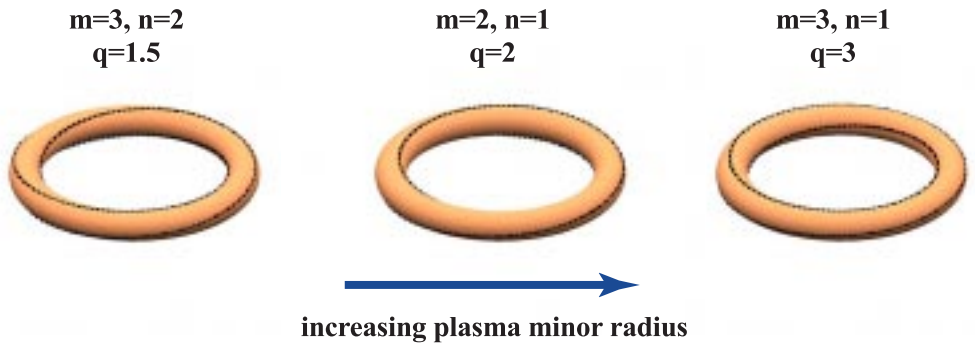

Figure 2.1: Magnetic field lines for various m and n numbers.

This relation implies that the magnetic islands form only on surfaces where the q value is a ratio of integers. The magnetic island adopts the same geometric structure as the rational surface field lines. The islands commonly encountered in tokamaks are illustrated in Figure 2.1. The standard notation describes the island using the m and n number of the rational surface as a ratio m/n. For example, the m=2, n=1 island at the q=2 surface is called the 2/1 island.

The current perturbation at the particular q surface produces the magnetic island. When the 2/1 island forms, the current separates into two channels. These channels

produce a poloidal field varying in strength and direction around the cross section. Magnetic diagnostics of m=2 islands use this variation to detect the presence of the island. The central points of the current perturbations are referred to as O-points, because the magnetic field around this point has a closed "O" shape. Correspondingly, the X-point is the location where the field lines from the separate current channels cross to form an "X" shape. These two points are the main focus of analysis in both experiments and theories. In the actual device, the perturbed current and field would be superimposed on the current and magnetic field from the rest of the plasma, creating a helical perturbation in the current and magnetic field.

Chapter 3. Magnetic Island Experiments on HBT-EP

Section 3.1. Introduction to the HBT-EP experiment

The HBT-EP (High Beta Tokamak – Extended Pulse) tokamak is an experiment studying the behavior and control of instabilities relevant to magnetic fusion [Mauel, in press; Navratil, 1998]. The experiment uses an array of diagnostics and an active rotation control system to study the behavior of magnetic islands. In particular, Mach probes extensively measured the pressure and velocity perturbations due to the magnetic islands.

For the HBT-EP experiment, the major radius of the plasma is typically $R \sim 94\,\text{cm}$ and the minor radius is $a \sim 13\,\text{cm}$. The average plasma density is $6\times10^{18}\,\frac{1}{m^3}$, while the peak temperature is around $150\,\text{eV}$. A system of capacitor banks supplies the currents for both forming the confining magnetic fields and drives the plasma current. These coils create a toroidal field of 0.34 T and drive 14 kA of current. Plasma current serves to both produce the poloidal field and heat the plasma. The vacuum chamber consists of 20 curved aluminum sections. Each section contains a pair of conducting shells as well as a number of ports for diagnostic and maintenance access. Two cryogenic pumps keep the base pressure in the UHV (ultra-high vacuum) region at $p \sim 2-6\cdot10^{-8}$ torr. During the plasma discharge pulse, deuterium gas is puffed to fill the chamber to a pressure of $p_{puff} \sim 2\cdot10^{-5}$ torr to form the plasma. A computer system controls the triggering of the plasma discharge and saves the data stored by the CAMAC digitizers into the MDS database.

Section 3.2. Active rotation control system

The key features for the study of magnetic islands on HBT-EP were the diagnostics and the external rotation control system. Magnetic islands create distinct perturbations in the magnetic field, with each type of island (2/1, 3/2, 3/1, etc.) possessing its own signature. This signature allows for the external detection of the internal island. In addition, the magnetic island structure resonantly interacts with external fields with the same structure. This allows the external control of the island velocity by imposing a rotating resonant magnetic perturbation (RMP) on the plasma. Changing the rotation rate of the RMP alters the island rotation. A system of external coils, with two 10 MW audio frequency amplifiers each driving a set of two coils pairs, creates the RMP. The coils are placed over quartz insulating breaks in the vacuum chamber. This allows the audio frequency fields to penetrate into the plasma while still using coils outside the conducting vacuum chamber. This system successfully changed the magnetic island frequency in a number of experiments [Mauel, in press; Navratil, 1998].

Section 3.3. Inductive diagnostics

A variety of diagnostics measure the plasma behavior. The first set of diagnostics makes inductive measurements of the currents, voltages, and magnetic fields in the plasma [Hutchinson, 1987]. A wire running toroidally around the tokamak measures the loop voltage drop V_{loop}. A Rogowski coil measures the toroidal plasma current I_p. Varying the density of the Rogowski coil winding according to

(3.1) $\sim \cos(m\theta)$ or $\sim \sin(m\theta)$,

allows the coil to measure plasma current perturbations with that particular m structure, creating a Fourier-analyzing Rogowski coil. The $m=1$ coils helps determine the vertical and horizontal displacement of the plasma current, and the $m=2,3$ coils observe the current perturbations from the formation of magnetic islands and various kink mode instabilities. The toroidal field B_ϕ is calculated from the current in the toroidal field coils, and the major radius R from the $m=1$ Fourier analyzing Rogowski coil. The minor radius a is calculated from the smallest value of the difference between the various limiter positions and the plasma major radius, and the poloidal field B_θ from the plasma current and minor radius. The q value at the edge of the plasma, referred to as q^* is

(3.2) $$q^* = \frac{aB_\phi}{RB_\theta}.$$

This value determines the highest q in the plasma. Finally, the current perturbation measurements from the Fourier-analyzing Rogowski coils are supplemented by shell mounted probes (SMP's) measuring the local perturbation in the poloidal field. A set of sixteen point coils mounted on the two conducting shells at one toroidal location provides poloidally-resolved measurement of magnetic island and kink mode magnetic field fluctuations.

Section 3.4. Plasma pressure diagnostics

The second set of diagnostics measures changes in the plasma density and temperature [Hutchinson, 1987]. A microwave interferometer operating at 94 GHz

measures the line-integrated density along a central chord. A single channel radiometer measures the radiated power over a wide viewing angle. Two multi-channel systems complement the single channel radiometer. The first system is a fan array of 16 soft x-ray detectors on a single IC package, viewing the plasma from a set of chords emerging from a single point. The fan array observes changes in the density and temperature due to both sawteeth oscillations and islands near the core of the plasma, such as the 3/2 magnetic island.

The second system is a tomographic array of 32 soft x-ray detectors. Each detector views a separate chord in vertical, horizontal, and diagonal directions. This system focuses on obtaining data to reconstruct the emission profile using techniques similar to those used in computed axial tomography (CAT) scans. The second main use is to detect soft x-ray fluctuations due to magnetic islands in the outer portion of the plasma, such as the 2/1 magnetic island.

Section 3.5. Physical layout of HBT-EP

Figures 3.1-3.2 illustrate the physical layout of the tokamak. Figure 3.1 is a top view of the experiment. A set of twenty large coils generates the toroidal field. The Ohmic heating coil in the center of the device drives the plasma current by acting as an air core transformer. The vacuum chamber sits inside the bore of the toroidal field coils. The UHV chamber has numerous ConFlat vacuum ports for diagnostic and pump system access to the plasma. Figure 3.2 schematically illustrates the layout, where the torus was cut toroidally along the inboard side, poloidally along the north edge of the device, and then flattened out. An angle convention allows for easy identification of positions on the

chamber. This system defines the poloidal angle zero point as the outboard side of the torus, with the top of the device at 90° and the inboard side at 180°. The zero point for the toroidal angle is at the north face of the tokamak, with the west face at 90° and the south at 180°.

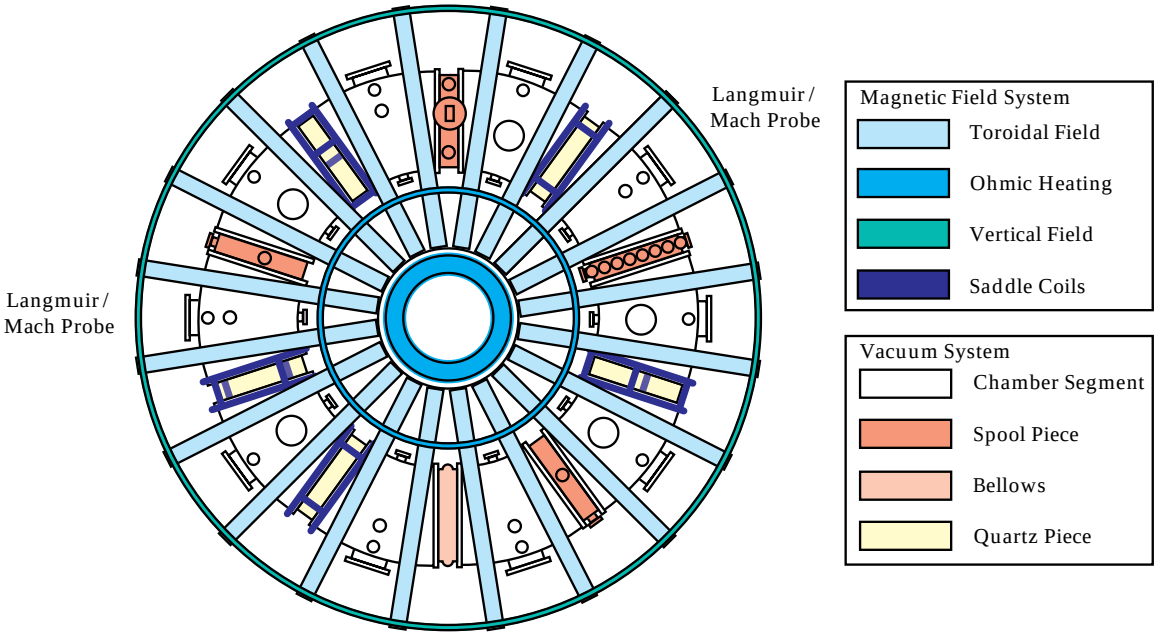

Figure 3.1: Top view of the HBT-EP tokamak.

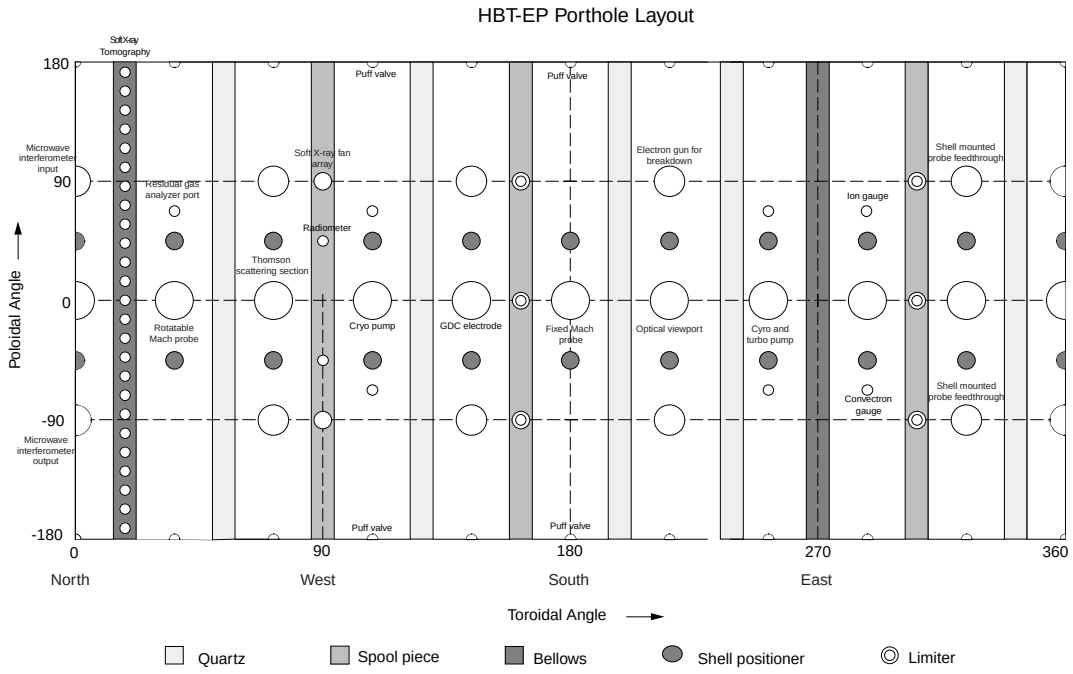

Figure 3.2: HBT-EP coordinate system.

Velocity measurements require a coordinate system to determine the sign of the velocity. The most convenient system would have positive velocity be in the same direction as the magnetic island motion, which is counter to the plasma current (Fig 3.3). An inward pointing radial electric field crossed with the poloidal magnetic field drives the fluid motion in this positive direction. The inward pointing pressure gradient drives ion flow in the negative and electron flow in the positive directions. Although the coordinate system defined earlier is very convenient from the lab perspective, a different system is more useful for dealing with the magnetic island and plasma fluid motion. In

the new system, the original poloidal angle θ is transformed to the new angle θ_{island} using

(3.3) $\theta_{island} = -\theta + \pi$.

This redefinition converts the outboard edge to 180° and the inboard side to 360° (Fig. 3.3). In the new system the island, ion fluid, and electron fluid move in the direction of decreasing toroidal and poloidal angle.

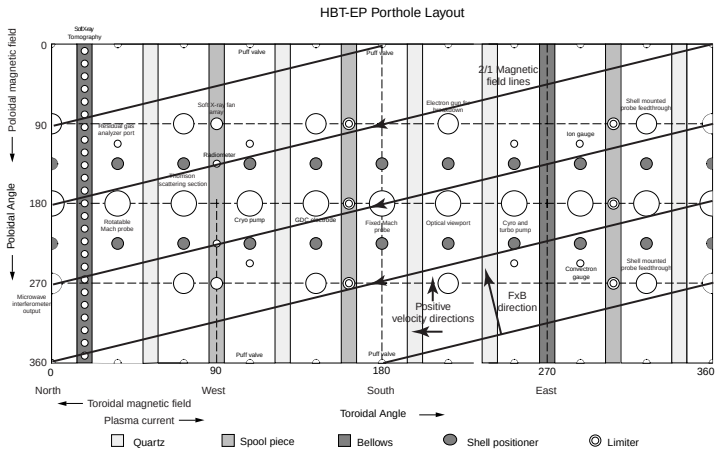

Figure 3.3: HBT-EP coordinate system for velocity measurements.

Section 3.6. Mach probe theory

The Mach probe [Hutchinson, 1987] is a directional version of the Langmuir probe [Hershkowitz, 1989] measuring the ratio of the ion velocity to the plasma sound speed. The electrode of the Langmuir probe is cut in half, separated by an insulator, and oriented orthogonal to the flow to produce an upstream and downstream electrode. This separation provides the directionality necessary to measure the velocity. The two probe

electrodes view different velocity distributions. The upstream electrode views a Maxwellian distribution of velocity shifted in the positive velocity direction, allowing the upstream probe to collect more current relative to stationary plasma. The opposite situation occurs for the downstream electrode. This electrode sees the plasma moving away from it with a Maxwellian distribution shifted in the negative velocity direction. Thus, the downstream electrode collects less current. A comparison of the upstream and downstream currents allows the determination of the plasma velocity.

The velocity is calculated using a theory developed by Hutchinson for the ion saturation current measured by probes in a strong magnetic field. This theory is for the flow along the magnetic field, which in a tokamak is effectively the toroidal direction. The Boltzmann relation for electron density is combined with the one-dimensional continuity and momentum equations. These equations include terms describing the density and momentum exchange between the region sampled by the probe and the rest of the plasma. An approximate solution to the system of equations is

$$\frac{n}{n_\infty} = \exp\left(M_\infty - M\right), \tag{3.4}$$

where n is the local density, n_∞ is the density far from the probe, M is the local Mach number and M_∞ is the plasma velocity far from the probe. The Mach number is defined as the ratio of the ion velocity to the ion sound speed

$$M = \frac{v_i}{c_s}, \tag{3.5}$$

$$c_s = \sqrt{\frac{T_e + T_i}{M}}\,. \tag{3.6}$$

Looking at the boundary between the pre-sheath and sheath regions, the upstream electrode measures a density n_{up} of

$$\frac{n_{up}}{n_\infty} = \exp\left(M_\infty - M\right), \tag{3.7}$$

while the downstream electrode measures n_{down}

$$\frac{n_{down}}{n_\infty} = \exp\left(-M_\infty - M\right), \tag{3.8}$$

where the plasma flow is in the opposite direction. Dividing these two equations cancels the local Mach number producing

$$\frac{n_{up}}{n_{down}} = \exp\left(2M_\infty\right). \tag{3.9}$$

When biased to a sufficient negative voltage, the upstream and downstream electrodes draw ion saturation current

$$I_{sat} = 0.6 \cdot A \cdot n \cdot \sqrt{T_e}\ . \tag{3.10}$$

Solving for n measured by the upstream and downstream probes and substituting into Equation 3.9 gives

$$\frac{I_{up}}{I_{down}} = \exp\left(2M_\infty\right), \tag{3.11}$$

where I_{up} and I_{down} are the ion saturation currents for the up and down stream probes respectively. Solving for the Mach number gives the relation

$$M_\infty = \frac{1}{2}\log\left(\frac{I_{up}}{I_{down}}\right), \tag{3.12}$$

which calculates the Mach number of the plasma, and in turn the ion velocity. Since the Mach probe is a Langmuir probe cut in half, it is reasonable to expect that adding both

the side probe signals together will reproduce the single probe behavior. The mean of the up and down stream electrode currents demonstrate little dependence on the Mach number, and reproduce the ion saturation current formula [Hutchinson, 1987].

Experiments in the KAIST tokamak reproduced the Mach number relationship between the ion velocity and ratio of the ion saturation currents [Yang, 1994]. Other theories exist for the interpretation of Mach probe signals, most notably the theory developed by Stangeby. The paper by Peterson summarizes and compares several of these models. However, the difference between the theories is significant only at large Mach numbers. For the typical range of Mach numbers on HBT-EP, the models converge.

Section 3.7. Mach probe system on HBT-EP

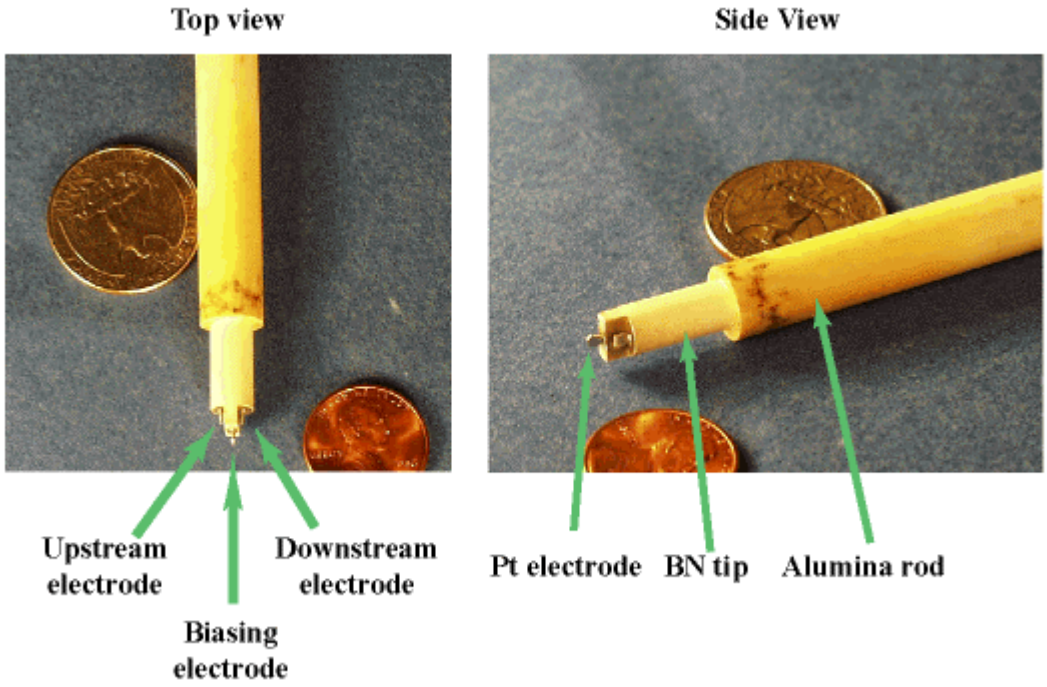

Figure 3.4: Mach probe layout.

Although Langmuir and Mach probes can provide a wealth of critical information on the plasma [Hershkowitz, 1989], the application of these diagnostics to tokamaks has largely been limited to the edge plasmas [Boedo, 1998; Howling, 1988; MacLatchy, 1992; Xiao, 1994]. The two main difficulties are the perturbation of the overall plasma behavior and melting of the probes. The probe system on HBT-EP overcame the perturbation issue by reducing the probe dimensions, and using a pair of probes at separate locations to measure the local perturbation from probe insertion. The melting problem was managed through the careful selection of material for the probe tip and electrode materials, as well as the operation of the system as a double probe to limit the current to the ion saturation level.

The probe assembly was designed to allow straightforward installation and replacement (Fig. 3.4). The electrodes were constructed of $1.0\,\text{mm}$ diameter platinum wire from Goodfellow Corporation. Platinum combines high temperature tolerance and low reactivity with a low secondary electron emission coefficient. Flattening the electrodes in a vise enhanced the directionality of the probe by creating a flat $0.017\,\text{inch}$ deep region with a height of $0.076\,\text{inch}$ and a width of $0.080\,\text{inch}$. A boron nitride tip housed the three electrodes. The probe was operated as a double probe, biasing the two side electrodes relative to the central electrode. Carborumdum supplied AX-05 Combat Grade Boron Nitride, the highest purity BN available, for the tip. Boron nitride is a machineable ceramic with high temperature and heat tolerances as well as good vacuum properties. Solvents should not be used to clean BN, as the material readily absorbs the liquids. Rather, baking the part at $600^{\circ}\,\text{F}$ removes fingerprints, oils, etc., from the material. Teflon coated wire was silver soldered to the electrodes and the three wires

were twisted so that the two side electrode wires wrapped around the biasing electrode wire. An eight-inch long alumina tube housed the probe tip assembly and wires. The tip was attached to the alumina using Resbond 907 Industrial Strength Fireproof Adhesive from Cotronics Corporation. The adhesive bonds ceramic materials and has been demonstrated with experience to be UHV compatible. At the end of the alumina tube connectors were soldered onto the wires, allowing the probe tip assembly to be installed or removed without disturbing the rest of the probe system.

The vacuum portion of the probe system allows the changing of the probe position between plasma shots. The probe tip assembly slides ~ 2 inches into a stainless steel shaft vacuum welded to a double-sided blank flange. Set screws hold the assembly in place, and the wires plug into connectors held in a Teflon plug. Teflon coated wire connects the plug to the electrical feedthrough. One of the probes includes a rotatable feedthrough from Kurt Lesker. The feedthrough allows the rotation of the probe about its long axis between shots while under vacuum, allowing measurements of both toroidal and poloidal plasma flows. A double pumped vacuum system maintains UHV conditions during probe rotation. It should be carefully noted that the screw holes on this feedthrough are tapped for metric screws. The other probe measured only toroidal motion. An edge-welded bellows from Standard Bellows Company contains the probe assembly and steel shaft. The bellows allows the probe to be inserted to near the center of the plasma and removed past a gate valve under UHV.

The electrical portion of the probe system performed the probe biasing and measures the current drawn by the plasma. The two side electrodes were connected to the negative terminal of a DC power supply. A diode was placed in series with the

negative terminal to prevent damage to the supply from reverse biasing. The biasing electrode was connected to the positive terminal. The typical bias voltage was $-150\,\mathrm{V}$. Rogowski coils from Pearson Electronics measures the current through each of the side electrodes. To reduce pickup of the vertical magnetic field, the coils where housed in aluminum Bud boxes. The output of the Rogowski coils was amplified, and the output digitized at $500\,\mathrm{kHz}$.

Section 3.8. Operation of the Mach probe diagnostic

An extensive number of tests verified the operation of the Mach probes. Unplugging one of the electrodes from the power supply and observing no change in the current drawn by the other electrode verified the biasing scheme. The directionality of the probe was verified using the rotatable feedthrough, rotating the probe 180° between shots. This act switched the signals measured on the probe electrodes for both toroidal and poloidal measurements, verifying the directionality. Placing both probes at the same major radial location demonstrated the agreement between the diagnostics.

The effect of the probes on the global and local plasma behavior determined their insertion limits. The presence of two separate probes allowed for the measurement of the local plasma perturbation. For $\frac{r}{a} > 0.692$, the location of the second probe produced no change in the other probe signal. Beyond this point, the downstream probe detected a decrease in the current drawn by the upstream electrode when placed at the same major radius as the other probe. However, the upstream probe at the same radial location did

not affect the downstream probe signal for $\frac{r}{a} > 0.692$. The limit on insertion due to arcing was $\frac{r}{a} = 0.577$. The probe limits are plotted in Fig. 3.5.

For magnetic island studies, key plasma parameters were held constant between the different shots. The plasma current, major radial position, edge q, loop voltage, m=2 and m=3 fluctuations, line integrated density, and central soft x-ray emissions were similar for the discharges. This was verified by comparing these quantities to those of shot 16982, which served as the standard for evaluating the quality of the discharge. After extensive clean-up shots, typical 2 out of 3 or 3 out of 5 shots would reproduce shot 16982. In total, this research encompassed shot numbers from the 12000's to the 19700's, or roughly 8000 shots.

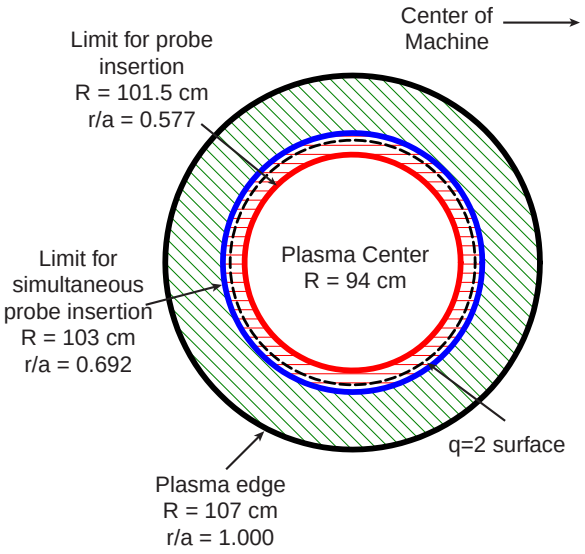

Figure 3.5: Poloidal cross-section illustrating the limits of probe insertion.

Chapter 4. Effect of Magnetic Islands on the Ion Velocity

Section 4.1. Magnetic islands, diamagnetism and neutral damping

The effect of magnetic islands on the pressure profile can potentially alter the ion motion by changing the diamagnetic velocity. The weaker electric fields and stronger neutral damping seen in tokamaks with Ohmic heating could allow this velocity term to play a significant role in determining the ion and electron fluid behaviors. Previous experiments demonstrated that magnetic islands could alter the pressure profile, and hence change the diamagnetic velocity. Two key velocity observations were made on the HBT-EP tokamak using the Mach probe system. First, the ion velocity profile had a large peak located near the center of the 2/1 magnetic island. Second, the ion velocity at this peak was significantly lower than the magnetic island velocity. These observations suggest that diamagnetic and neutral damping effects may contribute to the ion velocity. The inclusion of these effects could help explain the differences between the velocity and acceleration of magnetic islands and the nearby ion fluid seen in previous rotation control experiments on other tokamaks.

The fluid equations described in Chapter 2 outline the response of the ion and electron fluids to radial electric fields, pressure gradients, and neutral damping. Experiments on the TEXT tokamak demonstrated agreement between the predictions of these equations and the ion velocity [Rowan, 1993]. These experiments measured a reduction of the ion velocity due to the loss of momentum through charge exchange reactions with neutral particles [Rowan, 1993]. The damping factor developed for TEXT

would predict a reduction in the ion velocity of $F_{cx} \sim 30\%$ for a neutral fraction of particles of $n_n / n_{plasma} \leq 0.8\%$. The TEXT experiment also calculated the contributions to the ion velocity from radial electric fields and diamagnetism, supporting the validity of Eq. 2.14. However, the effects of magnetic islands were not included in the diamagnetic term. In addition, neutral damping could potentially alter not only the ion velocity but also the ion acceleration during active rotation control.

Magnetic islands can alter the fluid velocities by changing the pressure profile, and hence changing the diamagnetic velocity. Extensive experimental evidence shows that magnetic islands alter the plasma pressure profile. Experiments on the ORMAK tokamak [Vahala, 1980] tracked moving temperature perturbations using soft x-ray emissions and connected them to magnetic islands. Similar results were measured on the TEXTOR [deVries, 1997], RTP [VanMilligen, 1993], and TEXT [Brower, 1993] tokamaks and the W-7 stellarator [Jaenicke, 1988]. These experiments related density or temperature perturbations to the rotating magnetic island structure. Experiments on TFTR further demonstrated that changes in the pressure profile produced a corresponding change in the island growth [Chang, 1995]. These results demonstrate that magnetic islands interact with the pressure profile; however, they did not connect changes in pressure profile to changes in the ion velocity.

Section 4.2. Magnitude of the electric field term

The motion of the magnetic island, ion fluid, and electron fluid becomes straightforward to describe when the electric field is the dominant term in the velocity

equation. If few neutral particles are present so that $F_{cx} \sim 1$, and the electric field velocity is much larger than the diamagnetic velocity, $\omega_E >> \omega_{*_\alpha}$, Eq. 2.14 reduces to

(4.1) $\omega_\alpha = \omega_E$.

Since this velocity is independent of the mass and charge of the fluid particles, the ion and electron fluids will move at the same velocity.

This situation appeared in the DIII-D [LaHaye, 1993; LaHaye, 1994] and JET [Snipes, 1988] tokamaks, two of the largest tokamaks in the world. In the DIII-D device, the electric field term in the fluid velocity equations dominates over the negligible diamagnetic term, except at the extreme edge of the plasma, $r/a \approx 1$ [LaHaye, 1994]. The neutral beam heating system acted as a significant source of momentum, thereby increasing the radial electric field. In addition, the extensive plasma heating systems and good plasma confinement allowed the achievement of a fully ionized plasma, thereby reducing neutral damping effects. Static locking experiments demonstrated that stopping the island motion in turn brought the plasma velocity to near zero [LaHaye, 1994]. The large magnitude of the radial electric field, $< E_r >\sim 20 \frac{\text{kV}}{\text{m}}$ caused the ion and electron fluids, and in turn the magnetic island, to move at the same velocity. These results encouraged the acceptance of the assumption that the ion velocity is equal to the magnetic island velocity.

These conditions are not present in all tokamaks. Many smaller tokamaks and RFP's, similar in size to HBT-EP, measure radial electric fields on the order of $E_r \sim 1-7 \frac{\text{kV}}{\text{m}}$ [Xiao, 1994; MacLatchy, 1992; Antoni, 1996]. Diamagnetic terms can then play a significant role in determining the fluid velocities, as seen on the TEXT

experiment [Rowan, 1993]. In addition, smaller devices lack the $B_T \geq 2\,\mathrm{T}$ magnetic fields and extensive auxiliary heating systems of the large tokamaks. This reduces the density and temperature, which allows the penetration of neutral particles into the plasma. These neutral particles then in turn reduce the ion fluid velocity [Rowan, 1993]. These two effects can combine to separate the motion of the ion and electron fluids.

Section 4.3. Measurements of ion fluid and magnetic island velocities

The COMPASS-C [Hender, 1992] and JFT-2M [Oasa, 1995] tokamaks measured separate motion of the ion fluid and magnetic islands during active rotation control. The COMPASS-C experiment used a system of external coils to produce a stationary 2/1 magnetic island. The appearance of this stationary island reduced the ion velocity at the q~2 surface by $-7\,\mathrm{kHz}$. However, natural 2/1 islands rotated at about $14\,\mathrm{kHz}$, which would correspond to a change in the island velocity of $-14\,\mathrm{kHz}$. Hender attempted to explain this difference by attributing it to either a large shear in the velocity profile creating erroneous ion velocity measurements, or that the island flattened the pressure profile and hence reduced diamagnetic velocity. However, neither the ion velocity profile or pressure profile was presented as evidence.

The JFT-2M tokamak [Oasa, 1995] observed similar behavior during active rotation control experiments. Frequency ramp resonant magnetic perturbations succeeded in changing both the magnetic island and ion velocities. However, the acceleration experienced by the island was three times larger than that experienced by the ion fluid. One explanation offered suggested that the "no-slip" condition between the

island and the plasma might not always hold true. As demonstrated by the fluid equations, this is possible if pressure gradients and/or neutral damping are present.

Section 4.4. Models of the island effect on the diamagnetic velocity

Theoretical models suggested that the profile changes from magnetic islands alter the diamagnetic velocity. A two-fluid simulation of the effect of magnetic islands on the pressure calculated that the gradient inside the magnetic island would decay to near zero, $\nabla p \sim 0$, on the order of $\tau_R/10$, a tenth of the resistive time scale [Scott, 1985]. For HBT-EP, this time is $\sim 0.45\,\mathrm{ms}$, or approximately $1/16$ of the plasma shot length. Finn also performed a two-fluid plasma simulation demonstrating that magnetic islands alter the pressure profile, which in turn changed the diamagnetic velocity and hence the ion velocity [Finn, 1998]. These simulations differed, however, on the extent of the pressure flattening. In the Scott simulation the pressure flattened, $\nabla p \to 0$, over the entire magnetic island, while Finn determined that the flattening was a function of ratio of the ion sound speed to the Alfven speed for the propagation of magnetic fluctuations. For HBT-EP, this ratio is

$$\frac{c_S}{v_{Alfven}} \sim 0.03 . \qquad (4.2)$$

This value corresponds to a reduction of the pressure gradient over a portion of the island. Fitzpatrick determined a similar result using a diffusion-based model [Fitzpatrick, 1995]. Tokamaks the size of HBT-EP would not expect complete flattening of the pressure profile inside the magnetic island until the width is $\geq 3\,\mathrm{cm}$. These differing expectations

necessitate the measurement of both the pressure perturbations from the magnetic island, and the effect on the ion velocity profile.

Section 4.5. Magnetic island and ion fluid interactions

The HBT-EP tokamak offers the opportunity to demonstrate the importance of the interaction between magnetic islands and the ion fluid velocity. The effect of diamagnetism and neutral damping on the ion fluid velocity could potentially explain the difference between the ion fluid and magnetic island velocity observed on COMPASS-C and JFT-2M. HBT-EP observed similar velocity behavior as these tokamaks. Two features on HBT-EP suggest the presence of neutral damping and diamagnetic velocity effects from the magnetic island. Figure 4.1 plots the radial profile of the toroidal ion velocity. A large peak in the velocity profile occurs at the location of the 2/1 magnetic island. Localized pressure flattening would eliminate the local diamagnetic velocity, thereby increasing the local ion velocity. Figure 4.2 compares the velocity of the 2/1 magnetic island and the local ion fluid. Since the magnetic island moves with the electron fluid, this plot effectively compares the ion and electron velocities. The factor of three difference between the velocities could be explained by the presence of neutral damping. These two plots suggest that magnetic islands, through diamagnetism and neutral damping, play a significant role in determining the ion velocity.

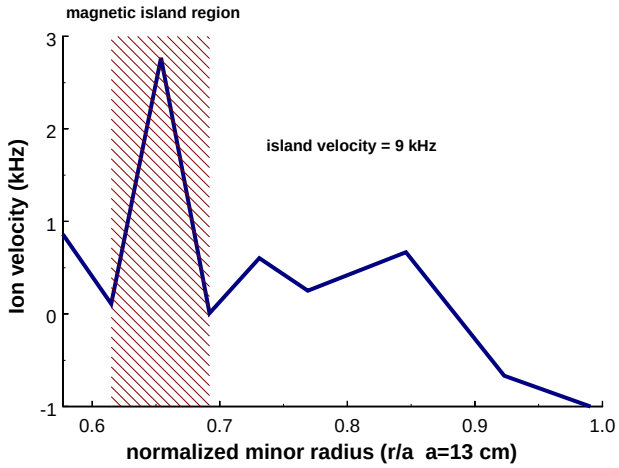

Fig 4.1: Radial profile of the toroidal ion velocity.

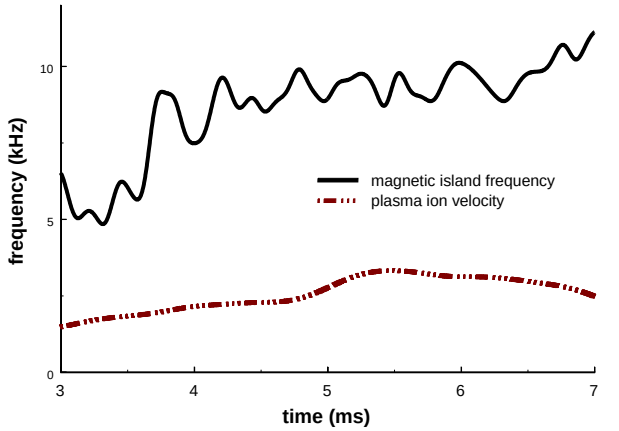

Fig 4.2: Time evolution of the ion fluid velocity and magnetic island velocity.

Three steps were used to understand the effects of magnetic islands and neutral damping on the ion velocity. First, a new technique based on the Hilbert transform was developed. This technique converted measurements of the rotating magnetic island with a stationary detector into a frame of reference co-rotating with the island. Next, this technique was applied to determine the radial pressure profiles of the O and X-points of the magnetic island. These profiles allowed the calculation of the diamagnetic velocity. Finally, this velocity, in conjunction with measurements of the neutral damping, was used to determine the contributions of diamagnetism, neutral damping, and electric fields to

the ion velocity profile. The results show that the peak in the ion velocity profile could be produced through changes in the diamagnetic velocity, and that neutral damping could be responsible for the factor of three reduction in the ion velocity as compared to the island velocity.

Chapter 5. Non-stationary Signal Analysis of Magnetic Islands

Section 5.1. Introduction

The measurement of rotating magnetic islands in the HBT-EP tokamak required a new data analysis technique to determine the frequency, amplitude, and phase of the rotating perturbations. In addition, a method was required to transform data from stationary detectors into the frame of reference of the magnetic island. Both these needs were met using the Hilbert transform.

Magnetic islands are common in a wide variety of magnetic fusion energy (MFE) devices [Sauter, 1997]. Magnetic islands generally rotate in these devices, creating perturbations that appear on diagnostics as a signal

(5.1) $$f(t) = a(t)\cos(\varphi(t)),$$

where $a(t)$ is the amplitude of the perturbation and $\varphi(t)$ is the phase. Figure 5.1 plots a typical signal, along with the amplitude, frequency, and phase of the signal. The time evolution the amplitude and frequency makes the calculation of the spectral quantities difficult. Standard analysis methods using discrete Fourier transforms [Bracewell, 1986] fail because of the time evolution, necessitating non-stationary signal analysis techniques in order to capture the island dynamics. The Hilbert transform offers an efficient and straightforward technique for calculating the time evolution of the amplitude, phase, and frequency of magnetic island perturbations. The Hilbert transform is extensively used in signal processing applications to determine the spectral quantities of signals from a

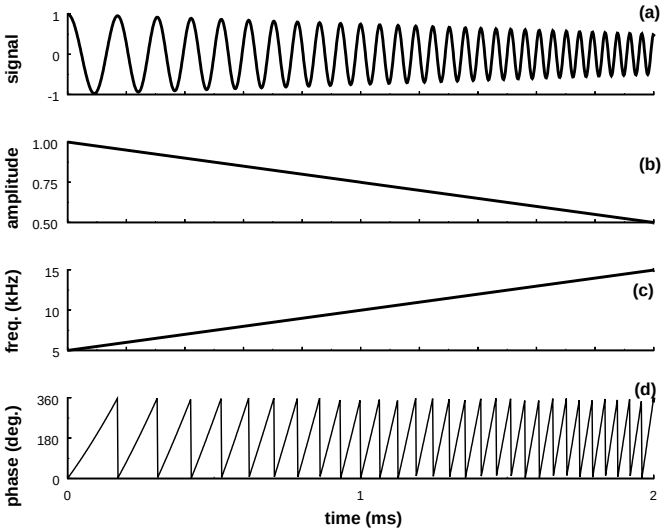

Figure 5.1: Example of a non-stationary signal. (a) is the signal, (b) is the amplitude, (c) is the frequency, and (d) is the phase.

variety of sources [Cohen, 1992; Cohen, 1995; Okunev, 1997]. The use of this transform in plasma physics has been largely limited to theoretical work. The Hilbert transform calculated the complex envelope of high frequency electromagnetic waves in plasmas in order to reduce the computational time and ease the comparison with theory [Ghizzo, 1995]. Another application calculated the Hilbert transform of a Gaussian function to produce the dispersion function, $Z(\xi)$, for waves in hot plasmas [Fried, 1961]. However, the application to magnetic island studies has been limited.

An importance focus of current magnetic fusion research is the control of magnetic islands with resonant magnetic perturbations (RMPs). These perturbations mimic the magnetic structure of the islands, providing an external means for interacting with the island. Synchronous RMPs act to reduce the island size through negative feedback, using the magnetic perturbation from the island as the input signal [Mauel, in press; Navratil, 1998; Morris, 1990]. Measurements of the island phase $\varphi(t)$ determine

the proper perturbation phase for producing negative feedback. Changes in the magnetic island amplitude $a(t)$ and the rotation frequency $\nu(t)$ measure the success of the feedback control. Asynchronous RMPs attempt to reduce the island size by changing the rotation frequency of the magnetic island [Mauel, in press; Navratil, 1998; Morris, 1990]. Theories predict that changes in the interaction between the magnetic island and the plasma will reduce the island amplitude [Boozer, 1996; Smolyakov, 1995]. Measurements of the island amplitude $a(t)$ and frequency $\nu(t)$ also judge the success of rotation control. Furthermore, since the success of the damping depends on the interaction with the plasma, the spectral response of plasma perturbations to rotation control also requires measurement. Finally, fundamental studies of island behavior focus on how the magnetic island structure interacts with the plasma [Finn, 1998; Fitzpatrick, 1995]. Since this structure rotates in experiments, diagnostics measure the island properties in the laboratory frame rather than the magnetic island frame of reference. Knowledge of the measurement phase allows the conversion to a frame of reference co-rotating with the island, providing data that can be more directly compared to theoretical predictions.

The importance of the amplitude, phase, and frequency in magnetic island studies led to the implementation of a wide range of techniques to determine these spectral quantities. The simplest technique tracks the maximum and minimum of magnetic signals to determine the location of the magnetic O and X points, respectively, of the magnetic island [deVries, 1997; VanMilligen, 1993]. A similar method tracks the zero crossing of the magnetic signals from spatially separated detectors to quantify the island propagation [Kluber, 1991]. The main weakness of these methods is that they ignore the

bulk of the data at the expense of only one or two points per cycle. Meaningful analysis requires lengthy time sampling with slow changes in the amplitude and frequency. The quadrature technique can also measure the spectral quantities of magnetic islands [Navratil, 1998]. However, this technique can only analyze signals that possess both a sine and cosine phase, limiting its application. Spectrogram analysis calculates the time history of the full Fourier spectrum of island signals [VanMilligen, 1993; Oasa, 1995]. The spectrogram generally wastes the bulk of the performed calculations for island studies, since normally the evolution of only one frequency component is of interest. The complex demodulation heterodyne technique reduces the number of calculations compared to the spectrogram, but retains information on the fundamental frequency and the harmonics of the island perturbation [Gasquet, 1997]. However, the method requires additional programming and the careful selection of a digital filter. The key advantage of the Hilbert transform method is that it offers a straightforward and efficient method for calculating the three spectral quantities from one signal. In addition, the transform is already implemented in many data analysis programs, such as IDL™ and MATLAB™, allowing the straightforward application to magnetic island data.

Section 5.2. Hilbert transform

This section summarizes the Hilbert transform properties relevant to magnetic island measurements. Determining the spectral quantities is simple if the quadrature component of the signal is known [Boashash 1992]. A quadrature signal is 90° out of phase with respect to the original signal. The quadrature component for 5.1 is

(5.2) $$g(t) = a(t)\sin(\varphi(t)) .$$

The combination of Eqs. 5.1 and 5.2 can determine the amplitude, phase, and frequency of the signal using the respective relations

$$a(t) = \sqrt{f^2(t) + g^2(t)}, \tag{5.3}$$

$$\varphi(t) = \tan^{-1}\left(\frac{g(t)}{f(t)}\right), \tag{5.4}$$

$$\nu(t) = \frac{1}{2\pi}\frac{d\varphi}{dt} = \frac{1}{2\pi}\frac{\frac{dg}{dt}f - \frac{df}{dt}g}{f^2 + g^2}. \tag{5.5}$$

Equations 5.1 and 5.2 can be combined to form the analytic function $s(t)$ [Cohen, 1992; Boashash, 1992]

$$\begin{aligned} s(t) &= a(t)e^{i\varphi(t)} \\ &= a(t)\left[\cos(\varphi(t)) + i\cdot\sin(\varphi(t))\right] \\ &= f(t) + i\cdot g(t). \end{aligned} \tag{5.6}$$

Using the analytic function, Eqs. 5.3-5.5 can determine the spectral quantities by taking the real and imaginary parts of $s(t)$ to get $f(t)$ and $g(t)$.

The Hilbert transform $H\{f(t)\}$ approximates the analytic function using only one input signal. The function is defined as [Cohen, 1995]

$$H\{f(t)\} = f(t) + i\cdot\int_{-\infty}^{\infty}\frac{f(t-\tau)}{\pi\tau}d\tau. \tag{5.7}$$

Unfortunately, multiple ways of analytically and numerically defining the Hilbert transform exist. This analytic definition differs from some formulas [Boashash, 1992] by the addition of the $f(t)$ term in order to make the function definition equivalent to the numerical implementation in MATLAB™. The transform is calculated numerically using fast Fourier transforms (FFT). The FFT of the signal is calculated, then the amplitude of

all the negative frequencies are set to zero. This modified FFT is then inverted to produce the Hilbert transform. The output of this Hilbert transform method approximates the analytic signal

(5.8) $$H\{f(t)\} \approx s(t) = a(t)e^{i\varphi(t)}.$$

Other numerical implementations of the Hilbert transform exist. One example is in IDL™ where for the default option the entire FFT transform is multiplied by the imaginary number i and then inverted. The output of this method is the negative of the quadrature signal, $-a(t)\sin(\varphi(t))$, rather than the analytic signal directly. The only significant difference between these and other methods is the exact process necessary to convert the Hilbert transform output into the quadrature signal. Once this process is determined, the different Hilbert transform methods are equivalent.

Two issues in the use of the Hilbert transform are the uniqueness of the output and how closely $H\{f(t)\}$ approximates the analytic signal $s(t)$ [Boashash, 1992]. The attempt to use one signal, the diagnostic data, to derive two signals, the amplitude and phase, creates the uniqueness problem. Changes in the oscillation behavior of $f(t)$ can be attributed to changes in either $a(t)$ or $\cos(\varphi(t))$. The Hilbert transform overcomes this difficulty by providing a well-defined algorithm for deriving two functions, $f(t)$ and $g(t)$, from the signal data. These two functions can then derive two more unique functions, the amplitude and phase, using Eqs. 5.3-5.4. Thus, the Hilbert transform will always produce a unique answer. This shifts the problem to whether the amplitude and phase behavior calculated with the two unique functions is meaningful.

Two conditions determine the accuracy of approximating the analytic signal with the Hilbert transform. These conditions place experimental requirements on the process

being measured. The first condition stems from the ambiguity about whether observed oscillations reflect changes in the amplitude or in the frequency. For the signal

(5.9) $f(t) = \cos(2\pi\nu_1 t)\cos(2\pi\nu_2 t)$; where $\nu_2 > \nu_1$,

the phase could be defined as $\varphi(t) = 2\pi\nu_2 t$ with the amplitude variation as $a(t) = \cos(2\pi\nu_1 t)$, or vice versa. The Hilbert transform overcomes this difficulty by selecting the higher frequency for the phase evolution [Cohen, 1995; Boashash, 1992]. Hence, the application of the Hilbert transform to Eq. 5.9 produces

(5.10) $H\{f(t)\} = \cos(2\pi\nu_1 t)e^{i(2\pi\nu_2 t)}$.

Thus, the amplitude variation in the signal must be slower than the island motion frequency. The second experimental condition states that the spectra of $a(t)$ and $\cos(\varphi(t))$ must be separated in frequency [Boashash, 1992]. Application of the Hilbert transform would place the slower variation into the amplitude and the faster into the phase, thereby mixing the two changes together and degrade the accuracy the calculated spectral quantities.

Magnetic islands generally meet these two conditions. The *m=2/n=1* islands on the HBT-EP (High Beta Tokamak – Extended Pulse) tokamak rotate with a frequency in the range of $\nu \approx 5-15$ kHz and an amplitude evolution of ≤ 2 kHz for both naturally rotating and externally controlled islands [Navratil, 1998]. These islands meet the condition that the amplitude variation is slower than the rotation frequency, and that the two spectra are separated in frequency.

Fourier analyzing *m=2* coils offer the opportunity to compare the Hilbert transform output to the actual analytic function. These coils detect the *m=2* magnetic

island and possess both a sine and cosine phase. The two signals can construct the analytic signal $s(t)$

(5.11) $s(t) = f_{\cos}(t) + i \cdot g_{\sin}(t)$,

where $f_{\cos}(t)$ is the cosine phase output and $g_{\sin}(t)$ is the sine phase output. Figure 5.2 compares the energy spectrum of $s(t)$ to the energy spectrum of the Hilbert transform of the cosine phase, $H\{f_{\cos}(t)\}$. The energy for both functions is concentrated in the positive frequency portion of the spectrum. The close agreement between the spectrums indicates that the Hilbert transform reproduces the analytic function. Since this implementation of the Hilbert transform sets the negative frequencies to zero, the lack of significant power levels at negative frequencies for the actual analytic function suggests that the Hilbert transform method accurately calculates this function.

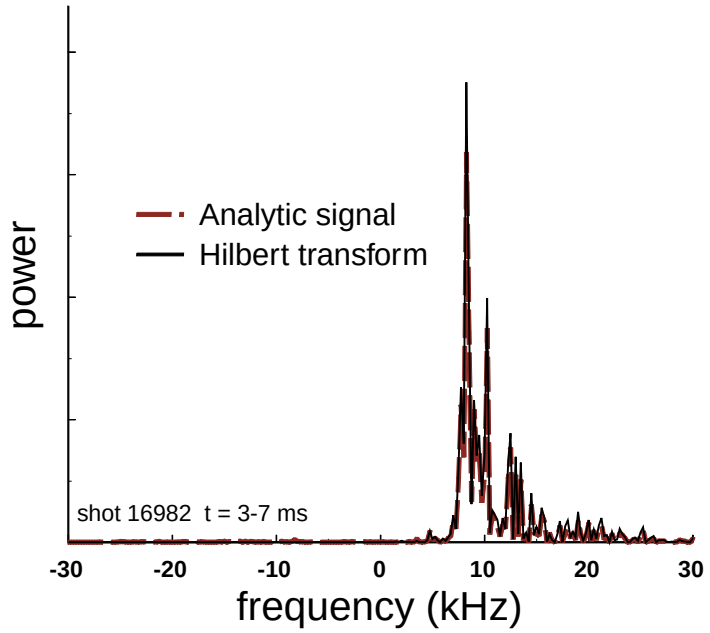

Figure 5.2: Comparison of the power spectrums of the Hilbert transform of the cosine signal from an m=2 detector and the analytic signal constructed from the cosine and sine signal.

The main exception to these conditions occurs during the locking of magnetic islands to stationary perturbations. Here, the island motion stops, bringing the frequency to zero. This slowing generally couples to a rapid growth in the island size [Scoville, 1991; Snipes, 1988]. The slowing of the island rotation and the increasing rate of island growth will eventually bring the frequency of rotation near that of the amplitude variation, violating the second condition. As the island motion ceases, the first condition will be violated. Nevertheless, rotation experiments focusing on changing the rotation frequency rather than locking the island motion will generally meet these conditions.

Section 5.3. Applications

Rotation control experiments on *m=2/n=1* magnetic islands in HBT-EP [Mauel, in press; Navratil, 1998] demonstrate the utility of the Hilbert transform. Resonant magnetic perturbations (RMPs) control the island rotation by resonantly interacting with the magnetic structure of the island. Changing the frequency of the perturbation changes the island rotation frequency. Figure 5.3 illustrates a typical RMP, where the frequency is ramped down from 15 kHz to 2 kHz , decelerating the island. An important issue in these experiments is the success of the RMP in changing the island motion. Indications of success appear in the frequency analysis of the magnetic island behavior. The magnetic perturbation from the island was windowed over two small time intervals, one early and one late in the ramp (Fig. 5.3b), then fast Fourier transformed. The motion of the peak frequency demonstrates that the RMP changed the island frequency. However, the most useful plot would directly compare the time evolution of the island frequency to that of the RMP. The Hilbert transform calculates this information in Fig. 5.3c,

illustrating the extent to which the RMP changes the island rotation. Because changes in the island rotation depend on a variety of plasma effects, this information is crucial to analyzing these experiments.

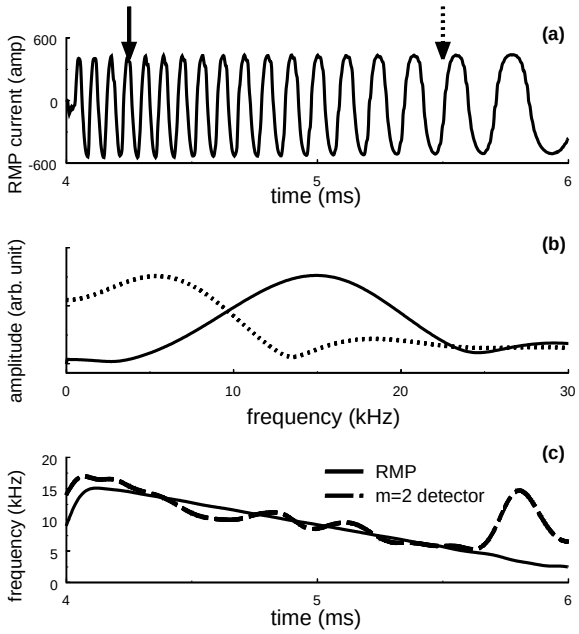

Figure 5.3: Rotation control experiment. (a) is the applied RMP. (b) is the frequency spectrum for data windowed around the points indicated by the arrows in (a). (c) plots the frequency for the RMP and the magnetic island.

A second application of the Hilbert transform compares the phase information of magnetic island data taken by diagnostics at different locations and/or measuring different properties. The phase difference between the diagnostic and the magnetic signal determines the location of the diagnostic measurement within the rotating magnetic island structure. This effectively moves the signal into a frame of reference co-rotating with the island. For example, a phase from the poloidal field measurement of zero could correspond to the magnetic O-point of the island, while a phase of $\pm\pi$ would in turn correspond to the X-point. One application determines the location of perturbations in the density within the island structure as measured by a microwave interferometer (Fig.

5.4). The lack of a quadrature signal for the interferometer, combined with the separate locations of the interferometer and magnetic diagnostics, makes direct interpretation of the phase difference between the perturbations difficult. The Hilbert transform straightforwardly calculates the phase of the interferometer and magnetic coil measurements. Removing the phase shift due to the different positions of these diagnostics determines the time-resolved phase difference (Fig. 5.4b). This phase difference is approximately zero, indicating that the density peaks occur in phase with increases in the poloidal magnetic field. This determines that the density is peaked near the island O-point.

This analysis can be extended to determining the behavior of a diagnostic signal in terms of the magnetic island structure. This application builds on the previous example. Rather than simply determining that the peak in the density occurs at the peak in the poloidal field, the entire density profile across the island can be calculated using the phase. The phase of the magnetic signal determines the location within the island of the measurement. Taking the phase of the magnetic signal, accounting for the phase shift due to the diagnostic positions, and then averaging over a small time interval produces a picture of the diagnostic measurement in terms of the phase of the magnetic signal (Fig. 5.4c). This allows for the study of the changes in the island structure across different discharge types, or for different diagnostic setups, such as different positions of Langmuir probes.

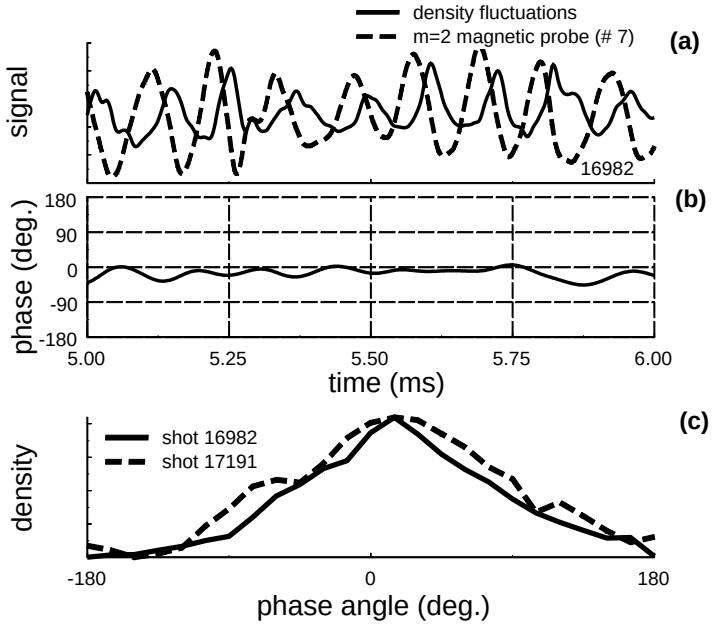

Figure 5.4: Phase calculations for magnetic and density perturbations. (a) plots the actual signals. (b) plots the phase difference, accounting for the detector locations. (c) plots the density as a function of island phase for two different shots.

Section 5.4. Comparison to other methods

The presence of a cosine and sine phase of the *m=2* coils allows the direct comparison of the Hilbert transform to exact quadrature calculations. The quadrature function $g(t)$ generated by the Hilbert transform (Eq. 5.6) can be directly compared to the actual quadrature signal $g_{\sin}(t)$ (Eq. 5.11) from the sine coil (Fig. 5.5a). The amplitude and phase from these two methods is compared in Figs. 5.5b and 5.5c. The Hilbert transform closely reproduces the actual quadrature function. The amplitude and phase calculated with the Hilbert transform in turn closely match the actual quadrature data. The key advantage of the Hilbert transform method is that only one signal is required to generate the amplitude and phase. The method is well suited for diagnostics

lacking a quadrature signal, such as Langmuir probes, soft x-ray detectors, and density measurements.

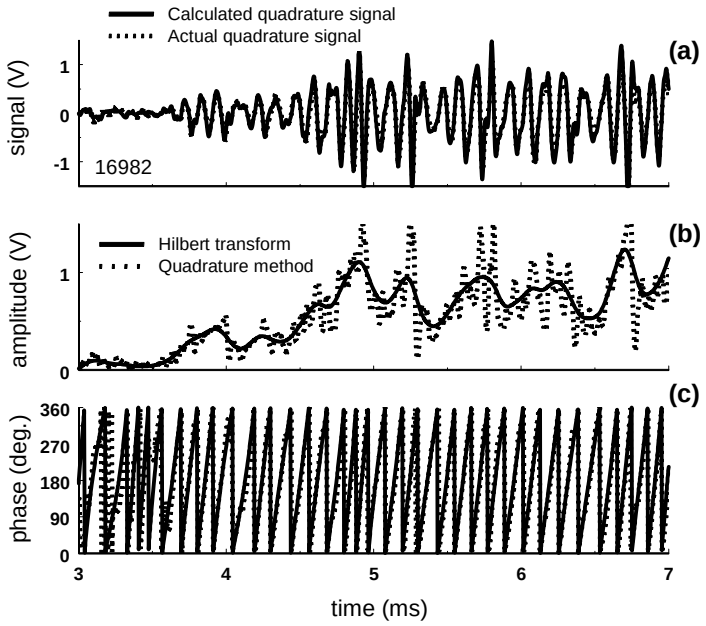

Figure 5.5: Comparison of the quadrature and Hilbert calculations of the (a) quadrature signal, (b) amplitude, and (c) phase.

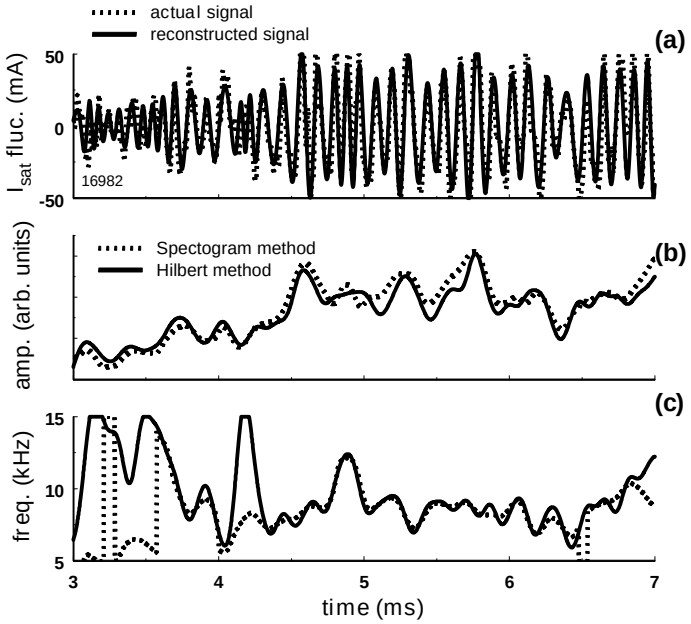

Figure 5.6: Comparison of spectrogram and Hilbert calculations of the (a) signal, (b) amplitude, and (c) frequency.

A common method used to determine the frequency and amplitude when no quadrature signal is present is the spectrogram, also known as the time-frequency distribution [Cohen, 1992]. A moving window generates the time-resolved frequency and relative amplitude, producing full frequency spectrum at each time point. Selecting the peak amplitude at each time point determines the time behavior of the dominant frequency and the relative amplitude. The application to ion saturation current measurements of island perturbations is plotted in Fig. 5.6. The amplitude and frequency demonstrate strong agreement between the two methods.

	Number of FFT's	Floating point operations
Hilbert transform	2	~15,000,000
spectrogram	2001	~880,000,000

Table 5.1. Comparison of the number of calculations for Hilbert transform and spectrogram processing of the data in Fig. 5.1.

There are two advantages of the Hilbert transform method over the spectrogram. First, the Hilbert transform is a significantly faster algorithm. Table 5.1 compares the number of FFT's and floating point operations required by both algorithms to analyze the same data. Generating the spectrogram required 1000 times more FFT's and approximately 60 times more floating-point operations than the Hilbert transform for the equivalent calculations. This saving translates into a significant increase in speed. The second advantage of the Hilbert transform stems from the ability to calculate both the phase and amplitude in the original signal units. Phase calculations using the spectrogram are unstable to small errors in the peak frequency. The small window required for high time resolution produces a large spread in the frequency domain, making selection of the peak frequency prone to small errors. However, the Hilbert

transform can robustly calculate the phase in the presence of error, as discussed in the next section. This allows for the simple reconstruction of the original signal from the calculated amplitude $a(t)$ and phase $\varphi(t)$

(5.12) $f_{\mathrm{r}}(t) = a(t)\cos(\varphi(t))$.

The reconstructed signal $f_r(t)$ can be directly compared to the original signal to determine the effect of the various filtering and smoothing operations (Fig. 5.6a). Spectral techniques invariably require filtering and/or smoothing of the signal, and the net effect on the spectral results is generally difficult to determine. A direct comparison of the original and reconstructed signal quickly highlights these effects. Furthermore, the comparison can also determine whether the signal behaves in a non-sinusoidal fashion, helping to determine when and how spectral techniques fail to fully describe the signal behavior.

The main disadvantage of the Hilbert transform method compared to the spectrogram is that the Hilbert method requires the signal to have only one dominant component. Signals of the form

(5.13) $f(t) = a_1(t)\cos(\varphi_1(t)) + a_2(t)\cos(\varphi_2(t)) + \ldots,$

where the amplitudes are on the same order of magnitude, $a_1 \sim a_2 \sim \ldots$, do not produce a meaningful amplitude and phase when calculated with the Hilbert transform, nor when calculated with quadrature techniques in general. Instead, the full spectrogram is required to individually trace the behavior of the various frequency components. When the diagnostic signal is dominated by oscillations from a single island structure, then the Hilbert transform may be generally used. More advanced techniques are required if the diagnostic signal contains information on multiple magnetic islands.

Section 5.5. Error analysis of the Hilbert transform

The Hilbert transform retains its ability to determine the amplitude and phase of a signal even in the presence of white noise and/or a lower amplitude signal component. The error due to white noise in the amplitude calculation is estimated by starting with the signal

$$f(t) = a(t)\cos(\varphi(t)) + \varepsilon_f(t), \tag{5.14}$$

where ε_f is the white noise in the signal. The quadrature component calculated with the Hilbert transform would be

$$\begin{aligned} g(t) &= \mathrm{Im}[H\{f(t)\}] = \mathrm{Im}[H\{a(t)\cos(\varphi(t))\} + H\{\varepsilon_f(t)\}] \\ &= a(t)\sin(\varphi(t)) + \varepsilon_g(t) \\ \varepsilon_g &= \mathrm{Im}[H\{\varepsilon_f\}]. \end{aligned} \tag{5.15}$$

Since the Hilbert transform only alters the phase of a signal, ε_g is essentially ε_f with the frequency components shifted by ninety degrees. Because the phase of white noise is random, both ε_f and ε_g possess the same noise amplitude. Thus, the error due to noise of both the original signal and its quadrature component is the standard deviation of the noise

$$\sigma \approx \text{std dev}(\varepsilon_f) \approx \text{std dev}(\varepsilon_g). \tag{5.16}$$

Calculating the error in the amplitude σ_{amp} using the standard formula for the propagation of errors [Mandel, 1984] gives

$$\sigma_{amp} = \sqrt{\left(\frac{\partial a}{\partial f}\right)^2 \sigma^2 + \left(\frac{\partial a}{\partial g}\right)^2 \sigma^2}$$

$$= \left[\left(\frac{f}{\sqrt{f^2+g^2}}\right)^2 + \left(\frac{g}{\sqrt{f^2+g^2}}\right)^2\right]^{\frac{1}{2}} \sigma = \sigma, \tag{5.17}$$

where the error in the amplitude is equal to the white noise error in the original signal.

A similar result holds when a second component is present in the signal. The signal detected is

$$f(t) = b(t)\cos(\varphi(t)) + c(t)\cos(\theta(t)), \tag{5.18}$$

where $b(t) >> c(t)$. The application of the Hilbert transform determines the "quadrature" signal

$$g(t) = b(t)\sin(\varphi(t)) + c(t)\sin(\theta(t)). \tag{5.19}$$

Calculating the amplitude using the condition $b(t) >> c(t)$ for a Taylor's series expansion gives

$$a(t) = \sqrt{f^2+g^2} = \sqrt{b^2+c^2+2bc\cos(\varphi-\theta)}$$

$$= \sqrt{b^2\left(1+\frac{c^2}{b^2}+2\frac{c}{b}\cos(\varphi-\theta)\right)} \approx b\left(1+\frac{c}{b}\cos(\varphi-\theta)\right) \tag{5.20}$$

$$\approx b + c,$$

where the maximum value of 1 was used for the cosine term. Thus, the error in the amplitude is on the order of the magnitude of the second component.

The Hilbert transform also accurately calculates the phase in the presence of signal error. Calculating the phase error for the signal in Eq. 5.14 gives

$$\sigma_\varphi = \sqrt{\left(\frac{\partial\varphi}{\partial f}\right)^2\sigma^2 + \left(\frac{\partial\varphi}{\partial g}\right)^2\sigma^2}$$

(5.21)

$$= \left[\left(\frac{-g}{f^2+g^2}\right)^2 + \left(\frac{f}{f^2+g^2}\right)^2\right]^{\frac{1}{2}}\sigma = \frac{\sigma}{b}.$$

Since the ratio $\frac{\sigma}{b}$ is the fraction of error in the signal in radians, a useful formula is

(5.22) $$\sigma_\varphi(\text{deg}) = \frac{\%}{100}\frac{180}{\pi} \approx \frac{2}{3}\%,$$

where % stands for the percent of white noise in the signal.

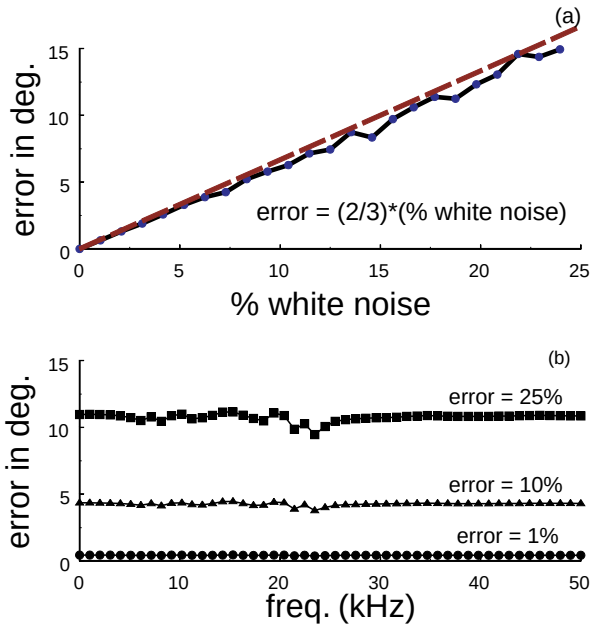

Figure 5.7: Error in the phase calculation for (a) white nose compared to the dashed line prediction of Eq. 5.22 and (b) a second frequency component scanned over a range of frequencies and amplitudes.

Figure 5.7 plots the effect of white noise and a second signal component on the phase calculation for the signal plotted in Fig.5.1. In Fig. 5.7a, white noise was added to the signal, and then the phase was calculated. This phase was compared to the phase of the base signal to determine the error. For white noise ranging from 0-25% of the signal

amplitude, the phase error ranges linearly from 0-15°. The calculated error is very close to the error estimate from Eq. 5.22. Figure 5.7b illustrates the effect of a second signal component. The phase $\theta(t)$ of the second signal component of Eq. 5.19 was selected to be $2\pi\nu t$. The phase was calculated, and then compared to the phase of the base signal $b(t)\cos(\varphi(t))$ at three different amplitude levels, ranging from 1% of the original signal up to 25%. This process was repeated by changing the frequency ν over the range from 0-50 kHz. The error in phase is independent of the frequency of the second component, and stays in the range of 0-15° for error amplitudes ranging from 0-25% of the original signal.

Section 5.6. Error analysis of the Mach probe signal

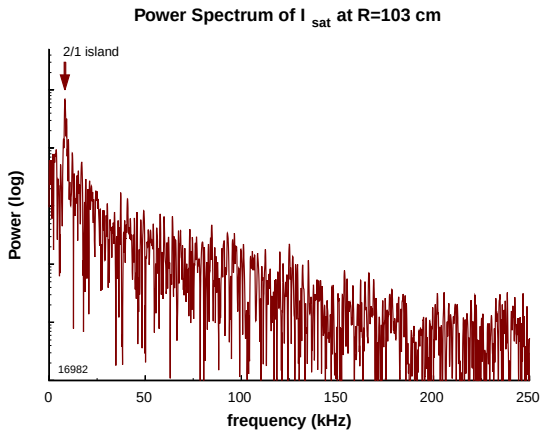

Figure 5.8: Power spectrum of the ion saturation current fluctuations.

The two main sources of fluctuations in the ion saturation current are magnetic island activity and turbulence. Figure 5.8 plots the power spectrum of the fluctuations in the probe signal. The behavior is very similar to behavior observed with Langmuir probes on a variety of tokamaks and RFP's [Fiskel, 1995; Boedo, 1998]. Magnetic islands drive the fluctuations at the peak frequency, while turbulence drives the

remaining fluctuations. The broad band turbulent spectrum decays with increasing frequency. For magnetic island studies, the signal from plasma turbulence not correlated to island activity, making it effectively equivalent to noise and the main source of error in island measurements.

The error incurred by turbulence can be estimated by comparing the probe signal to the signal reconstructed using the phase and amplitude information from the Hilbert transform. Since this spectral information reflects island activity, the difference between the signals is due to turbulence. This difference measures the error in ignoring the turbulent behavior. The probe signal is first run through a high-pass filter with a cutoff frequency of $1\,\mathrm{kHz}$ to remove the baseline, and smoothed with a $0.005\,\mathrm{ms}$ gaussian window to remove high frequency spikes. The Hilbert transform then calculates the phase and amplitude of the signal, which is used to reconstruct the signal. The deviation between the signals is calculated using

$$\sigma = \sqrt{\frac{\left(x_{signal} - x_{reconstruct}\right)^2}{N-1}} = 15\,\mathrm{mA}. \tag{5.23}$$

This value gives the error in a single probe measurement, which can then determine the error in the contour plots of the magnetic island profile. At each radial location, data from 2-3 shots over an $0.5\,\mathrm{ms}$ interval is placed into 24 angle bins and averaged. With the digitization rate of $500\,\mathrm{kHz}$, approximately 20 points go into each bin, giving an error of

$$\sigma_{contour} \approx \frac{\sigma}{\sqrt{N}} = 3\,\mathrm{mA}. \tag{5.24}$$

For the Mach number calculations, the error calculation is based on the formula [Mandel, 1984]

(5.25) $z = f(x, y, ...)$,

(5.26) $\sigma_z^{\,2} = \left(\frac{\partial f}{\partial x}\right)^2 \sigma_x^{\,2} + \left(\frac{\partial f}{\partial y}\right)^2 \sigma_y^{\,2} + ...$,

where z is the value calculated using $x, y, ...$ and the σ terms measure the error. The error in the Mach number is governed by

(5.27) $\sigma_{Mach}^{\,2} = \frac{\sigma_{up}^{\,2}}{4I_{up}^{\,2}} + \frac{\sigma_{down}^{\,2}}{4I_{down}^{\,2}}$,

(5.28) $\sigma_{up} \approx \sigma_{down} \approx \sigma$,

(5.29) $I_{up} \approx I_{down} \approx 40\,\text{mA}$,

(5.30) $\sigma_{Mach} = 0.05$.

Chapter 6. Pressure Perturbations from Magnetic Islands

Section 6.1. Introduction to pressure perturbations

Ion saturation current measurements on HBT-EP demonstrated the effect of magnetic islands on the pressure profile. The first step in this analysis was to connect probe fluctuations to magnetic island activity. These fluctuations followed the magnetic island behavior in amplitude, frequency, and phase. Voltage scans of the probes suggested that the ion saturation current perturbation is largely an increase in the local density. The probe perturbations were then converted into the island frame of reference using the Hilbert transform. This analysis generated contour plots of the time evolution of the magnetic island as a function of the phase angle of the magnetic perturbation and the minor radius. Examination of the O and X-points determined that the effect of the island is largest at the O-point, with limited perturbation at the X-point. This behavior is consistent with the presence of plasma compression by the magnetic island.

Section 6.2. Fluctuations in the ion saturation current

The ion saturation current measured the pressure perturbation due to the 2/1 magnetic island. The pressure is equal to the product of the density and temperature

(6.1) $p = nT$,

while the ion saturation current I_{sat} [Hershkowitz, 1989] is proportional to

(6.2) $I_{sat} \propto n\sqrt{T} = p/\sqrt{T}$.

Magnetic islands are the dominant source of ion saturation current fluctuations. I_{sat} fluctuations correlated with the $m = 2$ magnetic island activity detected with a Fourier analyzing Rogwski coil. Figure 6.1 illustrates this behavior, together with the behaviors of the $m = 3$ coil, the q^* value, and the major radial position of the plasma.

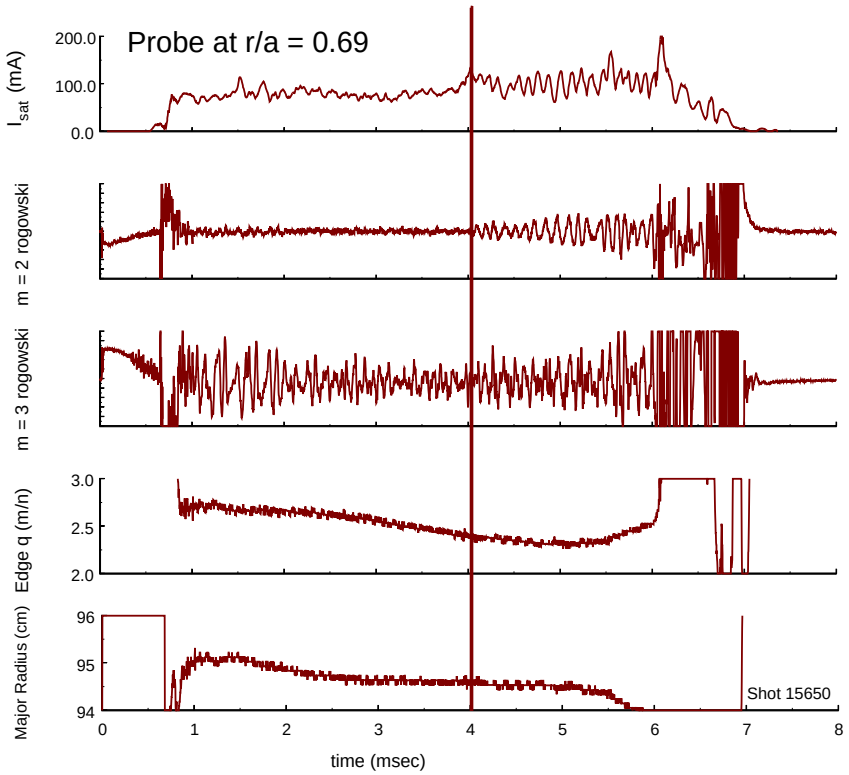

Figure 6.1: Correlation between m=2 and probe fluctuations. Plotted from top to bottom are the ion saturation current, m=2 signal, m=3 signal, edge q, and major radius of the plasma.

The ion saturation current has two distinct regions. The first region runs from $t \approx 1-4$ ms where the saturation current is roughly constant. At $t \approx 4$ ms, large, distinct fluctuations in the ion saturation current appear. These fluctuations coincide with the onset of 2/1 magnetic island activity observed on the $m = 2$ coil. The other signals remain relatively constant during the discharge. The stability of the position and q^*

indicate that the probe is measuring the same plasma. The $m = 3$ fluctuations did not correlate to the ion saturation behavior, suggesting that other island structures were not responsible for the probe perturbations. The correlation of fluctuations from the 2/1 magnetic island with the behavior of the ion saturation current indicates that the island produces the fluctuations.

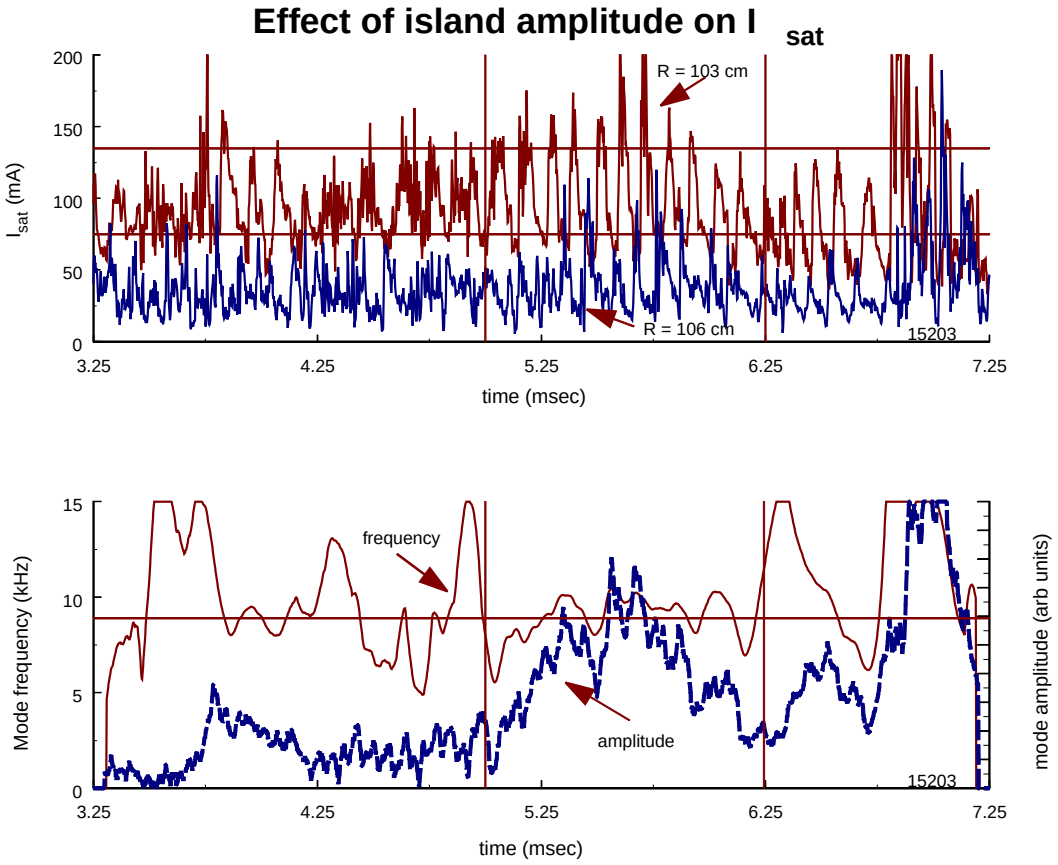

Figure 6.2: Top graph is the ion saturation current measurements at two different major radial positions. Bottom plot displays the magnetic island evolution during the same period.

The fluctuations in the ion saturation current are both localized near the island and follow its amplitude evolution. Figure 6.2 plots the ion saturation current measured at two different major radial positions in the same shot, one at $r/a = 0.7$ and the second closer to the edge at $r/a = 0.9$. Figure 6.2 also shows the magnetic island frequency and

amplitude evolution. During the early portion of the shot, the probes observe high frequency oscillations with little coherent structure. As the magnetic island amplitude increases at $t \sim 5\,\text{ms}$ the probe begins to detect coherent fluctuations at $r/a = 0.7$. These fluctuations follow the evolution of the island amplitude from $t \sim 5 - 6.25\,\text{ms}$. The probe at $r/a \sim 0.9$ does not measure fluctuations until later in the shot at $t \sim 6\,\text{ms}$ when the island amplitude is large. These results show that the fluctuations in the ion saturation current follow the magnetic island amplitude behavior and are spatially localized inside the plasma.

Finally, the success in attributing the ion saturation current fluctuations to the 2/1 magnetic island encouraged the comparison of the frequency, amplitude, and phase of the probe fluctuations to those of the magnetic field. The Hilbert transform was used to calculate the frequency, amplitude and phase of the two signals. The baseline offset and low frequency evolution were removed using a zero-phase digital filter. The data is filtered with a second order Butterworth highpass filter with the cutoff at $1\,\text{kHz}$, and then the data is reversed and run through the filter again. This process doubles the filter order without distorting the phase of the signal. The amplitude and the frequency (Figure 6.3) match between the two signals. Figure 6.3 also plots the phase difference between the two signals taking into account the phase shift due to the different diagnostic positions. The signals are in phase, with a stable phase difference over the shot. The phase calculation determines the location of the probe measurement within the magnetic island structure.

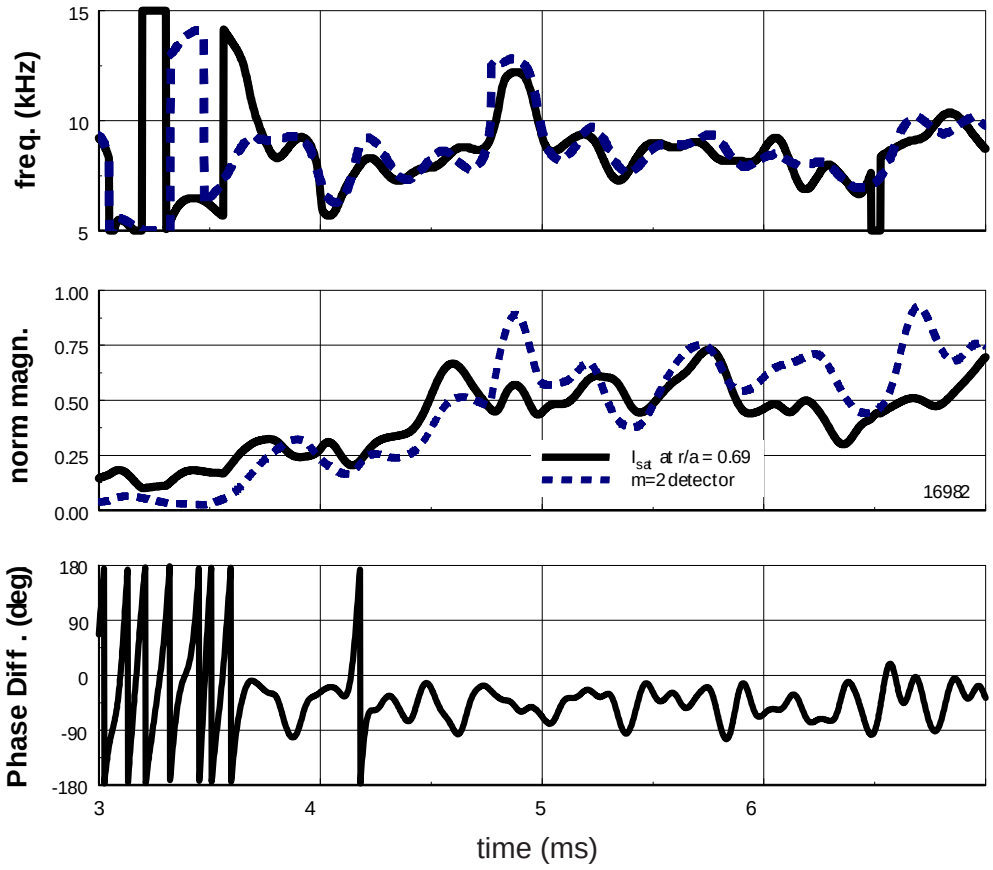

Figure 6.3: Frequency, magnitude, and phase difference between the ion saturation current perturbations and the magnetic island.

Section 6.3. Measurements of the fluctuation composition

The density and temperature of the island perturbation were determined by performing a current-voltage I-V scan of the probe. The probe bias was varied between shots, and then the resulting current measurements were converted into a frame of reference co-rotating with the magnetic island. The data near the island O-point and near the X-point were separately averaged for each voltage bias setting. Figure 6.4 plots the results. For a double probe system, the current I as a function of bias voltage V is [Hershkowitz, 1989]

$$(6.3) \quad I = \frac{qnA}{2}\sqrt{\frac{T_e}{M}}\tanh\left(\frac{qV}{2T_e}\right),$$

where q is the charge, A the area of the probe, n the plasma density, and T_e the electron temperature, and M is the ion mass. Figure 6.4 plots the I-V curves at a minor radius of 0.692 along with Equation 6.3 for two different values of n and T_e. When the island is saturated at $t = 5-6$ ms, the X-point is unperturbed by the island, while the O-point sees an approximate doubling of the density with a temperature of 45 eV. A similar analysis was applied at a minor radius near the edge, measuring a temperature of 15 eV.

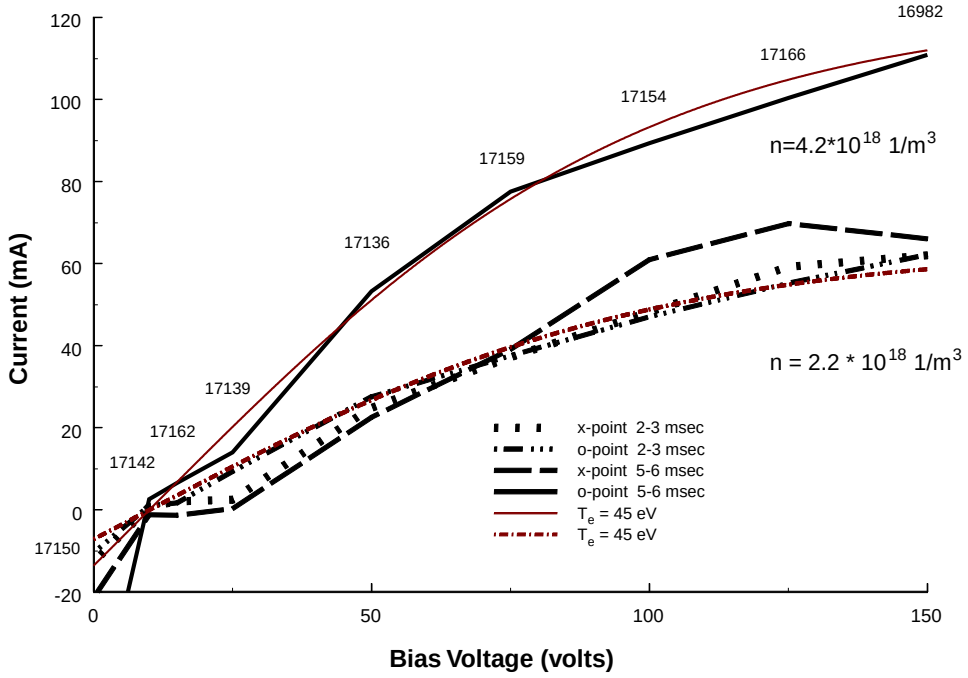

Figure 6.4: Effect of the magnetic island on the current-voltage behavior of the probe.

Section 6.4. Pressure fluctuations in the island frame of reference

The radial profile of the magnetic island perturbation can be converted into a frame co-rotating with the magnetic island using the phase measurements from the

Hilbert transform. This method allows the comparison to magnetic island theories, which state results in the island frame of reference. In particular, theories and experiments tend to focus on the O and X-point behavior. The toroidal rotation of the island past the stationary probe produces a toroidal picture of the magnetic island. The Hilbert transform calculated the phase of the probe measurements relative to the magnetic perturbation from the island structure. Data in $0.5\,\text{ms}$ intervals was sorted by angle then averaged in intervals of 15°. Each angle corresponds to a toroidal location co-rotating with the magnetic island. Figures 6.5-6.6 contain contour plots of the ion saturation current versus the minor radius and phase angle relative to the magnetic island O-point from $t = 3 - 7\,\text{ms}$.

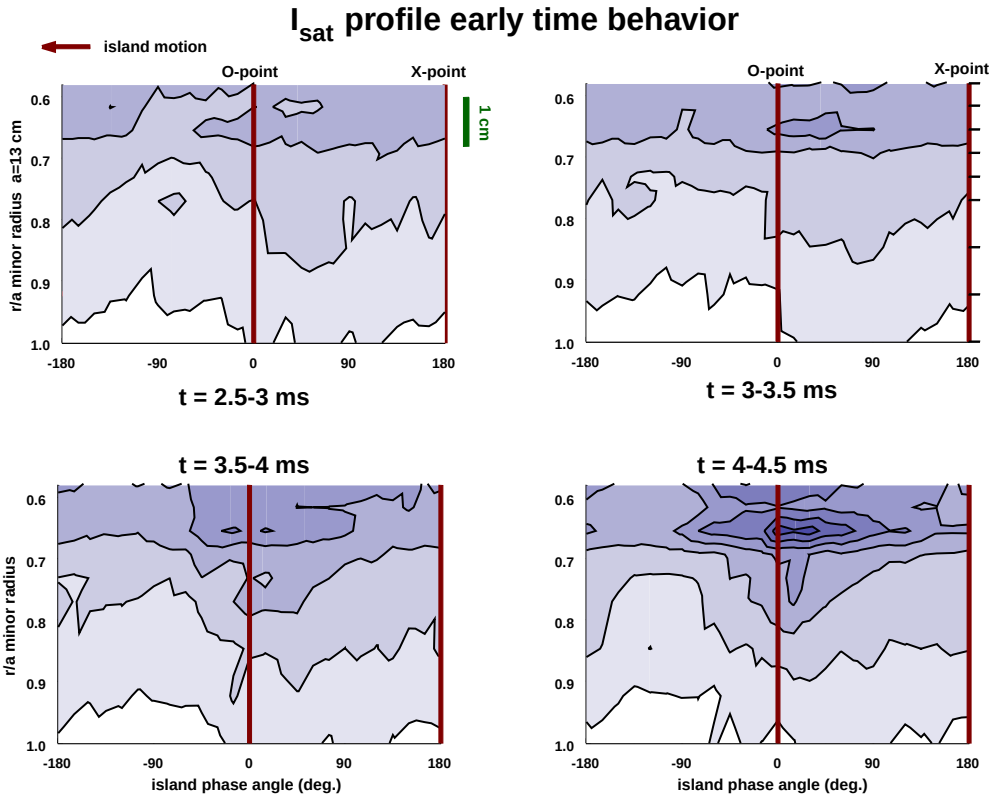

Figure 6.5: Contour plots of the ion saturation current as functions of minor radius and toroidal location within the rotating island structure. Each plot corresponds to a separate time interval.

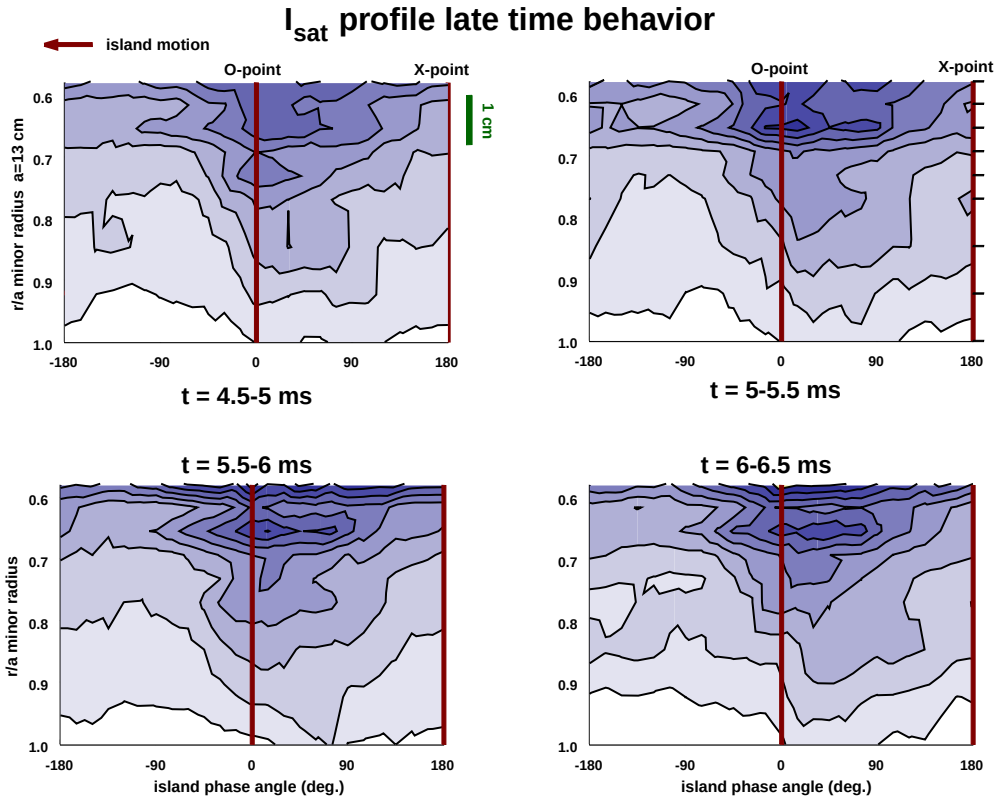

Figure 6.6: Same as Fig. 6.5 for later time periods.

major radius (cm)	r/a (a=13 cm)	shot number	probe
101.5	0.577	17757	rot (gain = 8)
		17370	rot
102	0.615	17740	rot
		19280	rot
102.5	0.654	17184	fix
		17185	fix
		17190	rot
103	0.692	16982	rot
		19294	rot
		17086	fix
		17730	rot
103.5	0.731	17197	fix
		17200	fix
104	0.769	17201	fix
		17203	fix
105	0.846	17204	fix
		17205	fix
106	0.923	16982	fix
		17206	fix
107	1.000	17100	fix

Table 6.1: List of shots used to construct the contour plots (Figs. 6.5-6.6). Probe column specifies the probe used: rot is the rotatable probe at a toroidal angle of 54°, and fix is the probe at 180°. The net gain was 20, except for shot 17757.

Early in the shot the small magnetic island makes a small perturbation centered at $r/a = 0.654$. As the island grows in amplitude during $t = 4-5\,\text{ms}$, the size and extent of the perturbation increases. Once the island saturates during $t = 5-7\,\text{ms}$, the perturbation remains constant.

These contour plots illustrate several key behaviors of the magnetic islands. The ion saturation current perturbation is centered at the island O-point at a minor radius of $r/a = 0.654$. The pressure perturbation decays both radially and toroidally from the island O-point. The size and extent of the perturbation both follow the behavior of the magnetic perturbation, featuring a small perturbation that grows over a 1 ms period and then saturates at a constant magnitude. The perturbation is not confined radially to the estimated island width of $1\,\text{cm}$, but rather extends over the entire outer minor radius.

Section 6.5. Behavior at the O and X-points of the island

Further information about the perturbation can be acquired by focusing on the behavior of the O and X-points of the magnetic island (Figure 6.7). Early in time at $t = 3-3.5\,\text{ms}$ there is little difference between the O and X-point radial profiles, matching the small island size. When the island has saturated at $t = 5.5-6\,\text{ms}$, the perturbation at the O-point increases in magnitude over the region between the magnetic island and the plasma edge. The X-point profile remains unchanged by the island growth. This behavior suggests that the pressure perturbation was largely confined to the region near the O-point.

The reconnection of the magnetic field at the O-point links regions of different pressure. This pressure gradient along the field line drives diffusion [Fitzpatrick, 1995] and/or sound waves [Scott, 1985; Finn, 1998] that average out the pressure gradient. The presence of a local maximum in the O-point profile indicates that the pressure gradient is zero over a small region of the magnetic island. A pressure gradient is still present over the rest of the profile.

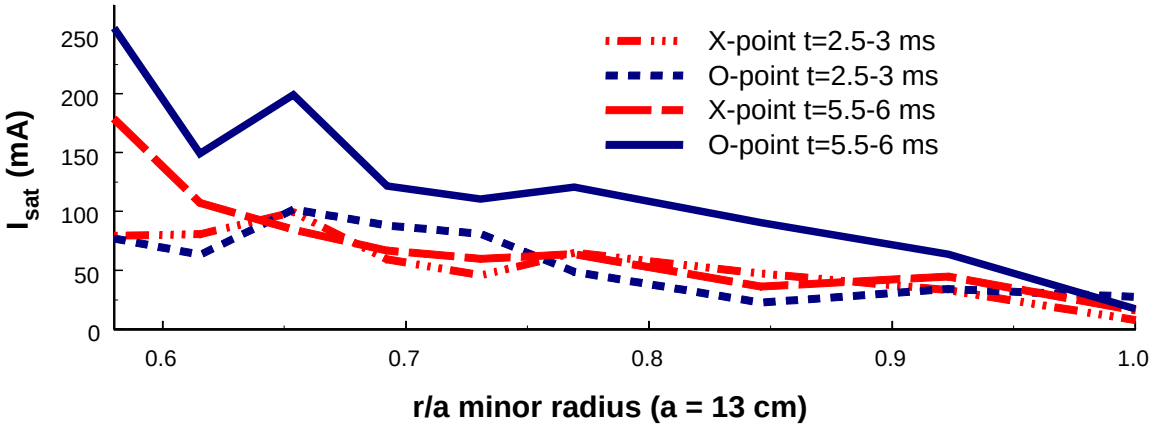

Figure 6.7: O and X-point radial profiles derived from the contour plots of the ion saturation current. The t=2.5-3 ms period is for a small magnetic island, and t=5.5-6 ms is for a large magnetic island.

This result agrees with predictions using both sound wave and diffusion theory. In the sound wave theory, the critical parameter for island flattening is the ratio of the ion sound speed to the toroidal Alfven speed, which on HBT-EP is

$$\frac{c_s}{v_{Alfven}} = 0.031. \qquad (6.4)$$

At low values of this parameter, the pressure gradient inside the island is reduced; however, this reduction need not extend over the full island width. The value for HBT-EP suggests that this is the case. For the diffusion model, only islands above a critical width produce full profile flattening inside the island. This width is a function of device size, and for HBT-EP is $w_{crit} = 3\,\mathrm{cm}$. Since the magnetic island is smaller than this size,

the island will not be completely flattened by diffusion. This may be compared to the predictions of Scott, which predict full flattening within the island. Taken together, these predictions state that the pressure will be flattened over a region less than or equal to the magnetic island size.

The radial extent of the pressure perturbation outside the magnetic island suggests the presence of plasma compression. A common assumption in magnetic island theory is that the island perturbation rapidly decays with increasing distance from the island [Fitzpatrick, 1995]. The profile at the O-point indicates that the pressure perturbation extents over the region from the magnetic island to the plasma edge. This perturbation was significantly larger than the theoretical assumption. Part of the perturbation could be due to compression of the outer plasma by the magnetic island. A simple compression model treats the magnetic island as a solid body that linearly displaces the plasma outwards. If the perturbation is due to compression, then the area under the O-point density profile from the edge of the island to the plasma edge should be equal to the area under the X-point profile including the island region. Because of the $m = 2$ nature of the perturbation, the island compression is more linear or slab-like than radial. A radial compression would best describe a $m = 0$ perturbation. The close agreement between these two numbers (Figure 6.8) suggests that the island compressed the plasma in the outer region.

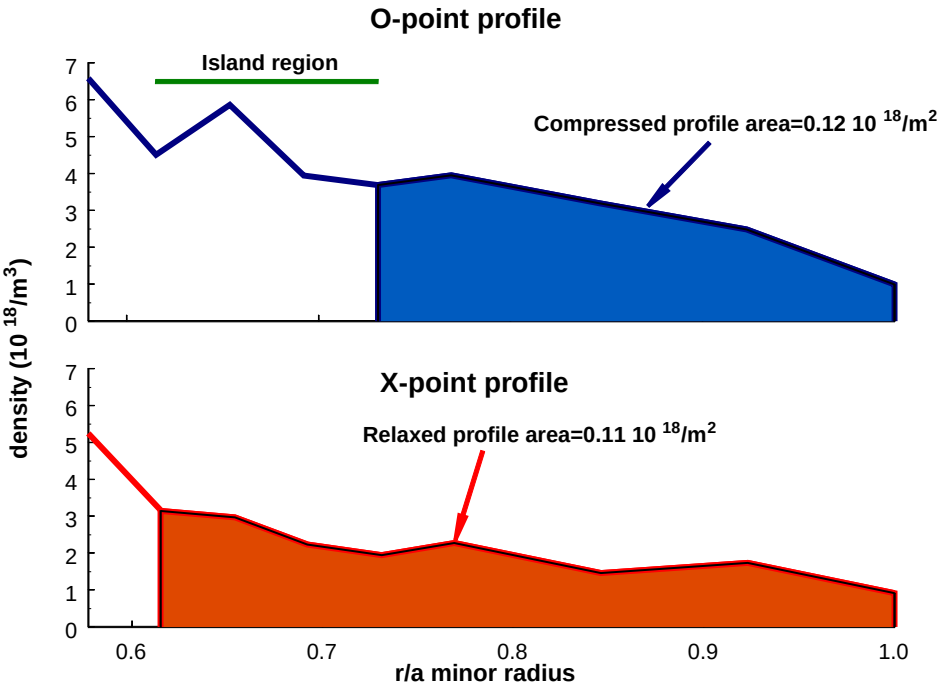

Figure 6.8: Presence of plasma compression in the density.

Section 6.6. Comparison to previous experiments

The measurement of the pressure perturbations from magnetic islands on HBT-EP extents the range of previous probe experiments. The ability to measure minor radial positions from $0.577 \le r/a \le 1.0$ substantially expands the range of observation. Previously, measurements of pressure perturbations from islands with probes were confined to the edge region of tokamaks [Howling, 1988]. Most other probe systems focused on turbulence measurements at the edge of different devices [Fiskel, 1995; Boedo, 1998; Uehara, 1998].

Application of the Hilbert transform to convert the data to a co-rotating frame complements multi-chord and multi-point measurements of the pressure perturbation. ECE [deVries, 1997; VanMilligen, 1993], tomography [Nagayama, 1996], microwave

interferometers [Brower, 1995], and Thomson scattering [Jaenicke, 1988] system measured the pressure profile perturbation using systems of multiple detectors at different minor radii. Reconstructing the island profile using the Hilbert transform eliminates the requirement for multiple, simultaneous measurements. Instead, information from one or two moveable detectors over multiple shots can determine the island pressure profile. This method significantly reduces the number of detectors required to produce the equivalent information.

Chapter 7. The Ion Fluid Velocity Profile and Two-fluid Model

Section 7.1. Effect of the island on the ion velocity

Chapter 4 highlighted the basic behavior of the ion fluid velocity. The two key experimental observations were the large increase in the ion velocity near the magnetic island, and the magnitude difference between the ion velocity and the magnetic island velocity. Experiments with active rotation control demonstrated that the acceleration experienced by the ion fluid is only 20% of that experienced by the magnetic island. Finally, the ion velocity has a fluctuating component near the center of the magnetic island. The observed ion velocity, as well as the rotation control and the fluctuating velocity measurements are consistent with a two-fluid model that includes diamagnetic and neutral damping effects.

Section 7.2. The diamagnetic velocity

The behavior of the ion fluid velocity is governed by Eq. 2.14

$$\omega_i = F_{cx}\left(\omega_E - \omega_{*_i}\right), \tag{7.1}$$

where ω_i is the ion velocity, F_{cx} is the neutral damping coefficient, ω_E is the electric field velocity, and ω_{*i} is the diamagnetic velocity. The results of the previous chapter measured the pressure profiles necessary for evaluating the ω_{*i} term. The diamagnetic term is

(7.2) $$\omega_{*i} = \frac{1}{2\pi R}\frac{1}{enB_p}\frac{\partial p_i}{\partial r}.$$

The temperature profile from the probe voltage scans allows the conversion of the ion saturation measurements into the plasma density. The pressure is derived from the density profile multiplied by the temperature profile

(7.3) $$p_i = n_i T_i .$$

Numerical differentiation calculates the profile gradient as a function of minor radius. The pressure perturbation at the center of the magnetic island varies on a distance scale smaller than the spacing between experimental measurements, making the numerical method inaccurate over this small region. The gradient at this point taken to be zero due to pressure flattening from the magnetic island. The local maximum in the pressure at the magnetic island implied that the local gradient is zero. This assumption agrees with observations in previous experiments [deVries, 1997] and theories [Scott, 1985; Finn, 1998; Fitzpatrick, 1995] of the island-pressure interaction.

Section 7.3. Neutral damping of the ion velocity

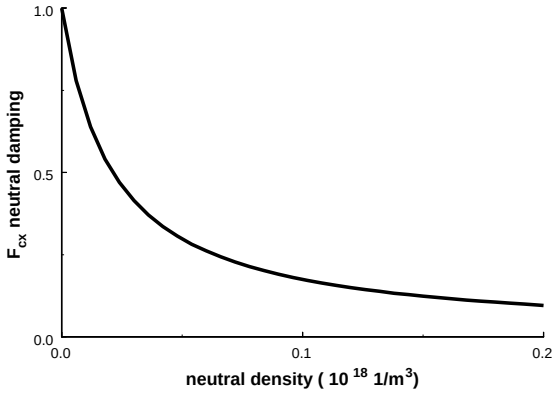

Figure 7.1: Dependence of neutral damping on the density of neutral particles.

Pressure flattening at the magnetic island also allows the calculation of the neutral damping term F_{cx} at the magnetic island. When the pressure gradient is zero, the diamagnetic term is zero, $\omega_{*i} \sim 0$, which reduces the velocity equation to

(7.4) $\omega_i = F_{cx}\omega_E$.

The electron velocity equation reduces to

(7.5) $\omega_e = \omega_{island} = \omega_E$.

The ratio of the two gives

(7.6) $\frac{\omega_i}{\omega_e} = F_{cx}$.

Magnetic island velocity measurements determine the electron velocity at the island location. This value, combined with the ion velocity, gives a neutral damping term at the magnetic island of

(7.7) $F_{cx} = 31\%$,

corresponding to a neutral fraction of $n_n / n_{plasma} \leq 0.8\%$. The profile of F_{cx} is calculated by estimating the fraction of neutral particles at the plasma edge. The chamber fill pressure of $p = 2 \cdot 10^{-5}$ torr gives a neutral density of $n_n / < n_e > = 10\%$, producing a neutral damping of $F_{cx} = 3.4\%$ (Fig. 7.1). A linear interpretation between these two points estimates the neutral damping profile.

Section 7.4. Contributions to the ion velocity

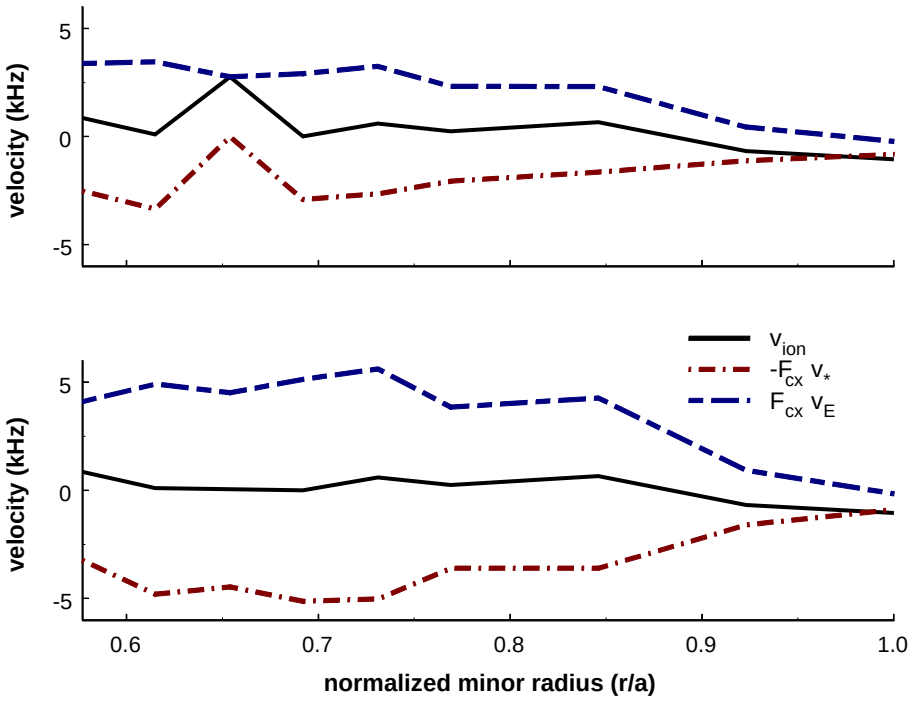

Figure 7.2: The diamagnetic, electric field, and neutral damping contributions to the ion velocity. Top plot includes the pressure and velocity perturbations from the island, and the bottom plot is with these perturbations removed.

The diamagnetic and neutral damping terms can be combined with measurements of ω_i to solve Eq. 7.1 for the ω_E term. Figure 7.2 plots ω_i, $F_{cx}\omega_E$, and $-F_{cx}\omega_{*i}$ as functions of the normalized minor radius. The large peak in the ion velocity is readily attributed to the elimination of the diamagnetic term inside the magnetic island. The neutral damping reduced the overall magnitude of the velocity terms. Examining the velocity profiles in the absence of the magnetic island further highlights the importance of the islands in determining the ion velocity profile. As shown in the previous chapter, the pressure perturbation due to the magnetic island is confined to the magnetic O-point. Thus, the X-point corresponds to the unperturbed pressure profile and can be used to calculate ω_{*i} without the island. The perturbation in the ion velocity is eliminated by

replacing the peak at $r/a = 0.654$ with the interpolated value from the surrounding data points. Figure 7.2 in the lower plot shows ω_i, $F_{cx}\omega_E$, and $-F_{cx}\omega_{*i}$ with the island perturbations in the pressure and velocity removed. The electric field and diamagnetic terms outside the island region are similar to the previous case. The key effect of the magnetic island is to locally flatten the velocity profile, eliminating the local diamagnetic velocity. This creates a distinct, local increase in the ion fluid velocity.

When the diamagnetic term goes to zero, the ion fluid moves at $F_{cx}\omega_E$, the electric field velocity multiplied by the neutral damping term. This behavior agrees with two-fluid simulations that predict pressure flattening inside the island. This flattening leads to the dominance of the electric field term in the velocity equation [Scott, 1985]. The limited radial extent of the velocity perturbation agrees with predictions of limited pressure profile flattening for plasma parameters typical of HBT-EP [Fitzpatrick, 1995; Finn, 1998]. Magnetic islands produce a distinct, localized perturbation in the ion velocity that is consistent with changes in the diamagnetic velocity term.

Section 7.5. Active rotation control

Rotation control provides an external means of altering the magnetic island motion [Mauel, in press; Morris, 1990; Navratil, 1998]. During frequency ramps, the frequency of the RMP (resonant magnetic perturbation) is linearly swept in time. The changing frequency of the RMP drives a changing island velocity, thereby accelerating the island. Figure 7.3 plots the frequencies of the RMP used for rotation control, the magnetic island, and the fluctuations in the ion saturation current. Neutral damping not only

reduces the magnitude of the ion velocity; it also may reduce the acceleration of the ion fluid during active rotation control.

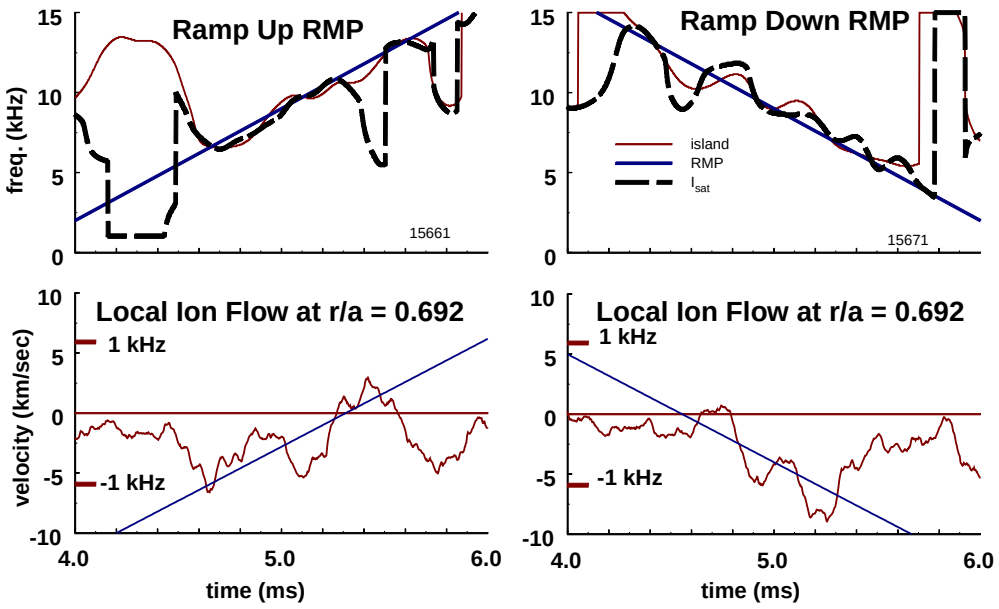

Figure 7.3: Effect of active rotation on the magnetic island, pressure perturbation, and ion velocity.

The pressure perturbation followed changes in the island frequency, indicating that this perturbation appears in the electron fluid rather than in the entire plasma fluid. The island and pressure perturbation frequencies are equal during the rotation control. Rotation control also successfully changed the ion fluid velocity (Figure 7.3). However, both the velocity and acceleration of the ions were less than that of the magnetic island, with the ion fluid acceleration being only 20% of the magnetic island acceleration. The rotation control can be modeled by placing an additional velocity term ω_{rot} in the equations for the ion and electron fluids. The equations then become, for the electrons and ions respectively,

(7.8) $\omega_e = \omega_E + \omega_{*_e} + \omega_{rot}$,

(7.9) $\omega_i = F_{cx}\left(\omega_E - \omega_{*_i} + \omega_{rot}\right)$.

Over the rotation control period, the diamagnetic, electric, and neutral damping terms remain constant. The time derivative of Eqs. 7.8-7.9 gives

(7.10) $$\frac{\partial \omega_e}{\partial t} = \frac{\partial \omega_{rot}}{\partial t},$$

(7.11) $$\frac{\partial \omega_i}{\partial t} = F_{cx} \frac{\partial \omega_{rot}}{\partial t}.$$

The ratio of the ion fluid acceleration (Eq. 7.10) over the electron acceleration (Eq. 7.11) equals F_{cx}. The acceleration ratio of 20% is on the order of F_{cx} measurements at the island (Section 7.2), suggesting that neutral damping may limit the external control of the ion velocity.

Section 7.6. Time evolution of the ion velocity profile

Mach probe measurements of the toroidal velocity profile observed a substantial effect from the presence of magnetic islands. The effect on the ion velocity profile is largely confined to the region near the island (Fig. 7.4). From $t = 1 - 4\,\text{ms}$, the plasma from $r/a = 0.577 - 1.00$ moves slowly in the plasma current direction. For $t \geq 4\,\text{ms}$, the velocities begin to diverge. This period coincides with the onset of magnetic island activity.

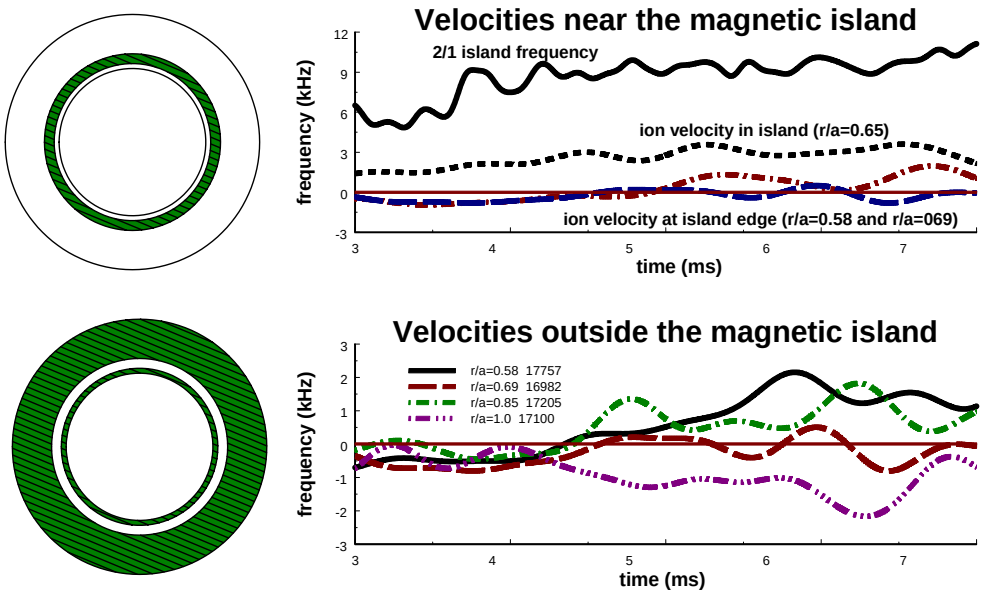

Figure 7.4: Ion velocity behavior both inside and outside of the magnetic island region. The graphs on the left show poloidal cross sections of the plasma, indicating the location of the velocity measurements.

The flow outside the island region ($\sim 0.5-1\,\mathrm{cm}$ from the resonant surface) at $t \geq 4\,\mathrm{ms}$ resembles the profile from TM-4, an earlier tokamak of similar parameters to HBT-EP [Bugarya, 1985]. TM-4 measured the ion velocity using the Doppler shift from impurity line radiation. The plasma velocity was highest in the core of the machine, and decayed with increasing minor radius. The velocity direction was counter to the plasma current direction (negative in the TM-4 coordinate system, and positive in the HBT-EP system). The velocity decayed to zero at a minor radius of $r/a \sim 0.6$, and then reversed direction. A similar behavior appeared on HBT-EP (Figure 7.4). The highest velocity occurred at the innermost probe measurement at $r/a = 0.577$ and decayed with increasing minor radius until the velocity reversed direction at $r/a \sim 0.65-0.75$.

Section 7.7. Fluctuating velocity component

The ion velocity also has a fluctuating component at the center of the island that follows the magnetic island motion. The previous discussions focused on the velocity behavior for time scales longer than the island rotation time. On shorter time scales, the velocity fluctuates at the magnetic island frequency. This fluctuating component is confined to the island region. The fluctuation produces a 2-3 kHz difference between the O and X-point velocities. Changes in the diamagnetic velocity could drive this fluctuation. Figure 7.5 plots the time evolution of the toroidal velocity as a function of radius and location in the magnetic island structure. From $t = 3 - 3.5\,\mathrm{ms}$ when the magnetic island is small, the fluctuations in the velocity are small and incoherent. Once the island saturates at $t = 5.5 - 6\,\mathrm{ms}$, large fluctuations at the O-point appear near the center of the magnetic island.

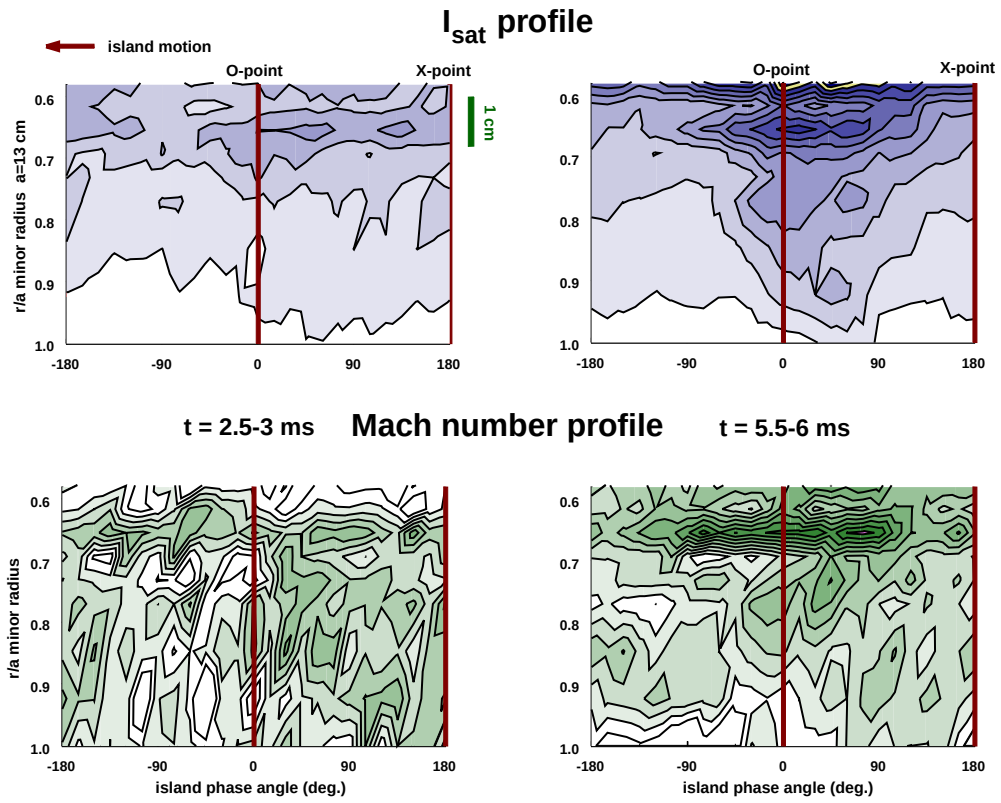

Figure 7.5: Contour plots of the ion saturation current and the toroidal Mach number for a small island at t=2.5-3 ms and a large island at t=5.5-6 ms.

Figure 7.6 illustrates the radial profile of the ion velocity at the O and X-points during the saturated island period. Pressure profile flattening near the center of the magnetic island can generate the peak in the velocity at the O-point. When the pressure gradient goes to zero, the diamagnetic velocity also goes to zero, resulting in an increase in the ion velocity. However, a pressure gradient remains at the X-point, resulting in a lower ion velocity at the same position. Figure 7.6 plots

(7.12) $\Delta\omega = -F_{CX}\left(\omega_{*_O} - \omega_{*_X}\right)$,

the difference in frequency $\Delta\omega$ between the diamagnetic frequencies at the O-point, ω_{*_O}, and the X-point, ω_{*_X}, multiplied by same neutral damping term F_{cx} used in Eq. 7.1. Equation 7.12 predicts a difference between the O and X-point velocities, similar to the experimental observations in Fig. 7.6. This behavior suggests that the pressure flattening is confined to a small region near the center of the magnetic island, and that changes in the pressure profile from the magnetic island produce corresponding fluctuations in the ion velocity, as predicted by Finn.

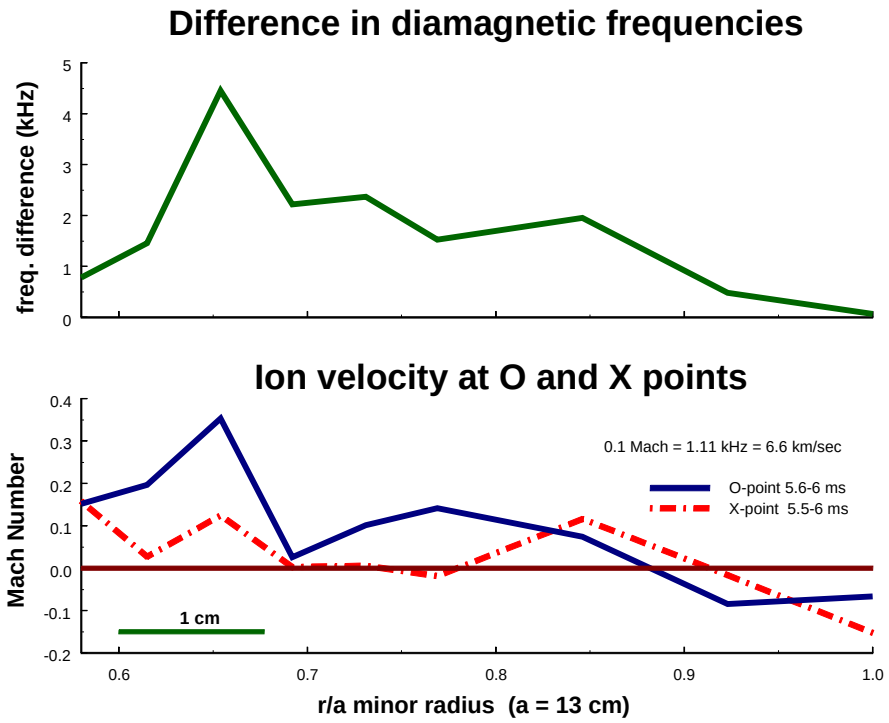

Figure 7.6: Difference between the diamagnetic velocity at the O and X-points, and the ion velocity measured at the O and X-points.

Chapter 8. Summary of Results

Section 8.1. New results

Magnetic islands are present over a wide range of fusion devices [Sauter, 1997]. These islands reduce the plasma confinement and hence the fusion performance. The prevalence of this instability over a wide range of fusion confinement schemes and experiments prompted the development of techniques to actively suppress magnetic islands. Active rotation control attempts to use the interaction between magnetic islands and the plasma for suppression [Navratil, 1998; Mauel, in press; Morris, 1990]. The success of this technique crucially depends on the details of this interaction [Boozer, 1996; Smolyakov, 1995]. Experiments on the HBT-EP tokamak using Mach probes served to locally measure the plasma perturbations in the pressure and ion velocity profiles from magnetic islands.

Magnetic island rotation creates rotating perturbations in the magnetic field, density, and temperature [deVries, 1997; Brower, 1995; VanMilligen, 1993; Jaenicke, 1988; Vahala, 1980; Kluber, 1991; Howling, 1988; Nagayama, 1996]. Understanding the behavior of these perturbations is critical to understanding the interaction between the magnetic island and the plasma. The time evolution of the amplitude and frequency necessitates non-stationary signal analysis techniques in order to capture the island dynamics [Bracewell, 1986]. The Hilbert transform calculated the amplitude, phase and frequency of the island signal from a single detector. Other techniques normally require systems of multiple detectors. The amplitude and frequency information helped

determine the success of active rotation control techniques in both changing the island motion and reducing its magnitude. The phase information allowed the straightforward comparison of diagnostics at different physical locations and measuring different plasma properties. Knowledge of the phase also allowed the conversion of the stationary diagnostic measurements to a frame of reference co-rotating with the magnetic island. This enabled the straightforward comparison of experimental results to theoretical predictions. The Hilbert transform method compares favorably both in speed and accuracy to spectrogram and quadrature methods of spectral calculations.

Ion velocity measurements determined that the ion fluid and magnetic islands have different velocities, as well as different accelerations under rotation control. The ion velocity profile is peaked at the island, with this peak velocity being less that the magnetic island velocity. This behavior is consistent with a two-fluid model that includes diamagnetic and neutral damping effects. Pressure flattening inside the magnetic island could eliminate the diamagnetic velocity term, increasing the ion velocity. The radial extent of this velocity perturbation is equal to or smaller than the magnetic island size, in agreement with theories predicting pressure flattening over only a portion of the magnetic island [Scott, 1985; Finn, 1998; Fitzpatrick, 1995]. Neutral damping can account for the large difference between the ion fluid and magnetic island velocities [Rowan, 1993]. This damping also can account for the reduction in the ion fluid acceleration during active rotation control. The combination of diamagnetism and neutral damping may help explain the complex velocity behavior observed on HBT-EP, and offers the potential to explain the ion and island motion observed on COMPASS-C [Hender, 1992] and JFT-2M [Oasa, 1995].

Probe measurements of the ion saturation current measured the perturbation in the pressure from the magnetic island. Pressure fluctuations followed the magnetic island behavior in amplitude, frequency, and phase for both naturally rotating and actively controlled islands. The Hilbert transform converted these measurements into a frame of reference co-rotating with the island. The pressure perturbation was confined to the island region near the O-point, with little or no effect at the X-point. The O-point profile displayed pressure profile flattening near the island center, and a pressure perturbation extending over the entire outer minor radius. Rotation control experiments demonstrated that the pressure perturbations move with the magnetic island and hence with the electron fluid.

Section 8.2. Ramifications for future work

The Hilbert transform offers an efficient and accurate method of calculating the amplitude, frequency, and phase of moving, localized perturbations from a single diagnostic. This novel application of the transform enabled a single probe to reproduce results similar to electron cyclotron emissions (ECE) and other multiple detector diagnostic systems [deVries, 1997; Brower, 1995; VanMilligen, 1993; Nagayama, 1996]. The phase information allowed the reconstruction of the magnetic island perturbation with a single moveable diagnostic and a reasonable number of plasma shots. This can be compared to ECE, which requires a large number of expensive detectors. This feature could translate into significant cost and design savings, and encourage more research into the use of moveable detectors for magnetic island studies. It also increases the usefulness of probes in island studies by reducing the size of the probe required to track the pressure

and velocity effects [Xiao, 1994]. Finally, the Hilbert transform can serve as the basis for improved island analysis methods. The success of its application to rotation control studies will hopefully drive the development of new methods for applications where the Hilbert transform assumptions are not met, particularly for island locking and stationary perturbation studies.

The results of the ion velocity measurements on HBT-EP are important to the treatments of plasma motion. In order for changes in the acceleration and velocity of the islands under active rotation control to equal that of the ion velocity, the electric field term must dominate the momentum balance equation. Measurements on HBT-EP indicate that this condition need not always be met. The presence of diamagnetism and neutral damping can separate the motion of the ion and electron fluids. The neutral damping term may reduce the velocity and acceleration of the ion fluid. Although active rotation control successfully changed the island and electron fluid motion [Mauel, in press; Navratil, 1998; Morris, 1990], ion velocity control in these regions may require a different technique to produce large changes.

The interaction between the magnetic island and the plasma highlight the need for further measurements of the effect of islands on the pressure and velocity profiles. Measurements of the effect of the island at the O and X-points have determined different results on different machines [deVries, 1997; VanMilligen, 1993; Jaenicke, 1988]. This behavior suggests the need for improved models that account for the differences between the devices, and highlight the need to measure, rather than simply assume, what the island effect on the pressure profile is. Velocity measurements suggest the interaction between the island and pressure profile can in turn alter the ion velocity. Pressure

flattening near the island can produce a local increase in the ion velocity. Changes in the pressure gradient and density at the O and X-points can also produce fluctuations in the ion velocity. These factors highlight the need for models such as the one developed by Finn, which combine the effects of the islands on the pressure and velocity profiles.

Understanding the effect of magnetic islands on the pressure and ion velocity profiles is crucial for both fundamental plasma studies and the development of more efficient tokamaks using advanced tokamak (AT) concepts. For fundamental studies, magnetic island research can provide the means to test theories about the interaction between magnetic fields and the ion and electron fluids. AT design concepts [Najmabadi, 1995; Stambaugh, 1995] depend on the ability of active rotation control to suppress magnetic islands and resistive wall modes [Garofalo, 1999]. An understanding of how the magnetic islands, pressure and velocity profiles, and external control systems interact is required to insure the successful operation of new tokamak designs.

Chapter 9. References

- M. Annaratone, T. Shoji, H. Maeda, et al., Nucl. Fusion **34**, 1453 (1994).
- A. V. Antoni, D. Desideri, E. Martines, Nucl. Fusion **36**, 1561 (1996).
- R. J. Armstrong, D. S. Darrow, Nucl. Fusion **34**, 1532 (1994).
- Glenn Bateman, *MHD Instabilities*, (MIT Press, Cambridge, 1978).
- M. G. Bell, Nucl. Fusion 19, 33 (1979).
- J. Boedo, D. Gray, L. Chousal, et al., Rev. Sci. Instrum. **69**, 2663 (1998).
- Allen H. Boozer, Phys. Plasmas **3**, 4620 (1996).
- Boualem Boashash, Proc. IEEE **80**, 519 (1992).
- Boualem Boashash and Graeme Jones, in *Time-Frequency Signal Analysis*, edited by Boualem Boashash (John Wiley & Sons, Inc., New York, 1992), Chap. 2.
- C. Boucher, C. S. MacLatchy, G. LeClair, et al., J. Nucl. Materials **176 & 177**, 1050 (1990).
- Ronald Bracewell, *The Fourier Transform and Its Applications* (McGraw-Hill, New York, 1986), Chap. 12.
- S. I. Braginskii, in *Reviews of Plasma Physics I*, edited by M. A. Leontovich, (Consultants Bureau, New York, 1965), p. 205.
- D. L. Brower, S. C. McCool, J. Y. Chen, et al., in *Plasma Physics and Controlled Nuclear Fusion Research 1992*, Proceedings of the 14th International Conference (International Atomic Energy Agency, Vienna, 1995), Vol. 2, p. 177.
- V. I. Bugarya, A. V. Gorshkov, S. A. Grashin, et al., Nucl. Fusion **25**, 1707 (1985).
- Z. Chang, J. D. Callen, E. D. Fredrickson, et al., Phys. Rev. Lett. **74**, 4663 (1995).
- Francis Chen, *Introduction to Plasma Physics and Controlled Fusion*, (Plenum Press, New York, 1984).
- Leon Cohen, in *Time-Frequency Signal Analysis*, edited by Boualem Boashash (John Wiley & Sons, Inc., New York, 1992), Chap. 1.

- Leon Cohen, *Time-Frequency Analysis* (Prentice-Hall, New Jersey, 1995), Chap. 2.
- P. C. deVries, G. Waidmann, A. J. H. Donne, F. C. Schuller, Plasma Phys. Control. Fusion **38**, 467 (1996).
- P. C. deVries, G. Waidmann, A. Kramer-Flecken, et al., Plasma Phys. Control. Fusion **39**, 439 (1997).
- P. C. deVries, A. J. H. Donne, S. H. Heijnen, et al., Nucl. Fusion **37**, 1641 (1997).
- P. C. deVries, Ph.D. thesis, University of Utrecht, 1997.
- A. V. Eletsky, B. M. Smirnov, in *Handbook of Plasma Physics Volume 1: Basic Plasma Physics I*, edited by A. A. Galeev and R. N. Sudan (North-Holland Publishing, New York, 1983), Chap. 1.2.
- John M. Finn, Phys. Plasmas **5**, 3595 (1998).
- G. Fiskel, S. C. Prager, P. Pribyl, et al., Phys. Rev.Letters **75**, 3866 (1995).
- Richard Fitzpatrick, Phys. Plasmas **2**, 825 (1995).
- Burton D. Fried and Samuel D. Conte, *The Plasma Dispersion Function* (Academic Press Inc., New York, 1961), Chap. 1.
- J. Friedberg, *Ideal Magnetohydrodynamics*, (Plenum Press, New York, 1987).
- T. Fulop, Peter J. Catto, P. Helander, Phys. Plasmas **5**, 3398 (1998).
- R. F. Gandy, J. Cooney, D. Forester, et al., Phys. Plasmas **5**, 2405 (1998).
- A. M. Garofalo, A. D. Turnbull, E. J. Strait, et al., Phys. Plasmas **6**, 1893 (1999).
- H. Gasquet and A. J. Wootton, Rev. Sci. Instrum. **68**, 1111 (1997).
- A. Ghizzo, T. Réveillé, P. Bertrand, et al., J. Comput. Phys. **118**, 356 (1995).
- David J. Griffiths, *Introduction to Electrodynamics*, (Prentice Hall, New Jersey, 1989).
- D. J. Den Hartog, J. T. Chapman, D. Craig, et al., Phys. Plasmas **6**, 1813 (1999).
- T. C. Hender, R. Fitzpatrick, A. W. Morris, et al., Nucl. Fusion **32**, 2091 (1992).
- Noah Hershkowitz, in *Plasma Diagnostics Volume 2*, (Academic Press, New York, 1989).
- S. P. Hirshman, D. J. Sigmar, Nucl. Fusion **21**, 1079 (1981).

- A.A. Howling, D. C. Robinson, Plasma Phys. Control. Fusion **30**, 1863 (1988).
- I. H. Hutchinson, Phys. Fluids **30**, 3777 (1987).
- I. H. Hutchinson, *Principles of Plasma Diagnostics*, (Cambridge University Press, New York, 1987).
- R. Jaenicke, W VII-A Team, Nucl. Fusion **28**, 1737 (1988).
- T. H. Jensen, A. W. Leonard, A. W. Hyatt, Phys. Fluids B **5**, 1239 (1993).
- O. Klüber, H. Zohm, H. Bruhns, et al., Nucl. Fusion **31**, 907 (1991).
- G. Kurita, T. Tuda, M. Azumi, T. Takeda, Nucl. Fusion **32**, 1899 (1992).
- R. J. LaHaye, R. J. Groebner, A. W. Hyatt, J. T. Scoville, Nucl. Fusion **33**, 349 (1993).
- R. J. LaHaye, C. L. Rettig, R. J. Groebner, et al., Phys. Plasmas **1**, 373 (1994).
- C. S. MacLatchy, C. Boucher, D. A. Poirer, et al., Rev. Sci. Instrum. **63**, 3932 (1992).
- C. S. MacLatchy, C. Boucher, D. A. Poirier, et al., J. Nucl. Materials **196-198**, 248 (1992).
- John Mandel, *The Statistical Analysis of Experimental Data* (Dover Publications, Mineola, NY, 1984), p. 74.
- M. E. Mauel, J. Bialek, C. Cates, H. Dahi, D. Maurer, D. Nadle, G. A. Navratil, M. Shilov, and E. Taylor, in *Plasma Physics and Controlled Nuclear Fusion Research 1998,* Proceedings of the 17th International Conference, Yokohama (International Atomic Energy Agency, Vienna, in press).
- W. Morris, T. C. Hender, J. Hugill, et al., Phys. Rev. Lett. **64**, 1254 (1990).
- Y. Nagayama, G. Taylor, E. D. Fredrickson, et al., Phys. Plasmas **3**, 2631 (1996).
- F. Najmabadi, ARIES team, in *Plasma Physics and Controlled Nuclear Fusion Research 1996*, Proceedings of the 16th International Conference, Montreal (International Atomic Energy Agency, Vienna, 1995), Vol. 3, p. 383.
- G. A. Navratil, C. Cates, M. E. Mauel, D. Maurer, D. Nadle, E. Taylor, Q. Xiao, W. A. Reass, and G. A. Wurden, Phys. Plasmas **5**, 1855 (1998).
- K. Oasa, H. Aikawa, Y. Asahi, et al., in *Plasma Physics and Controlled Nuclear Fusion Research 1994*, Proceedings of the 15th International Conference, Seville (International Atomic Energy Agency, Vienna, 1995), Vol. 2, p. 279.

- Yuri Okunev, *Phase and Phase-Difference Modulation in Digital Communications* (Artech House, Boston, 1997), Appendix.
- B. J. Peterson, J. N. Talmadge, D. T. Anderson, et al, Rev. Sci. Instrum. **65**, 2599 (1994).
- William L. Rowan, A. G. Meigs, E. R. Solano, et al., Phys. Fluids B **5**, 2485 (1993).
- O. Sauter, R. J. LaHaye, Z. Chang, et al., Phys. Plasmas **4**, 1654 (1997).
- George Schmidt, *Physics of High Temperature Plasmas*, (Academic Press, New York, 1979).
- Bruce D. Scott, A. B. Hassam, J. F. Drake, Phys. Fluids **28**, 275 (1985).
- J. T. Scoville, R. J. LaHaye, A. G. Kellman, T. H. Osborne, R. D. Stambaugh, E. J. Strait, and T. S. Taylor, Nucl. Fusion **31**, 875 (1991).
- A. I. Smolyakov, A. Hirose, E. Lazzaro, et al., Phys. Plasmas **2**, 1581 (1995).
- J. A. Snipes, D. J. Campbell, P. S. Haynes, T. C. Hender, M. Hugon, P. J. Lomas, N. J. Lopes Cardozo, M. F. F. Nave, and F. C. Schüller, Nucl. Fusion **28**, 1085 (1988).
- R. D. Stambaugh, V. S. Chan, R. L. Miller, et al., in *Plasma Physics and Controlled Nuclear Fusion Research 1996*, Proceedings of the 16th International Conference, Montreal (International Atomic Energy Agency, Vienna, 1995), Vol. 3, p. 395.
- P. C. Stangeby, Phys. Fluids **27**, 2699, (1984).
- Thomas H. Stix, Phys. Fluids **16**, 1260 (1973).
- K. Uehara, T. Kawakami, H. Amemiya, et al., Nucl. Fusion **38**, 1665 (1998).
- G. Vahala, L. Vahala, J. H. Harris, Nucl. Fusion **20**, 17 (1980).
- P. M. Valanju, M. D. Calvin, R. D. Hazeltine, and E. R. Solano, Phys. Fluids B **4**, 2675 (1992).
- P. Van Milligen, A. C. A. P. Van Lammeren, N. J. Lopes Cardozo, et al., Nucl. Fusion **33**, 1119 (1993).
- J. A. Wesson, R. D. Gill, M. Hugon, et al., Nucl. Fusion **29**, 641 (1989).
- John Wesson, *Tokamaks*, (Clarendon Press, Oxford, 1997).
- C. Xiao, K. K. Jain, W. Zhang, A. Hirose, Phys. Plasmas **1**, 2291 (1994).
- J. C. Yang, S. H. Seo, G. C. Kwon, et al., Physics Letters A **185**, 428 (1994).

- M. Yokoyama, J. D. Callen, C. C. Hegna, Nucl. Fusion **36**, 1307 (1996).